PCCP

ROYAL SOCIETY OF CHEMISTRY

PAPER

Published on 28 September 2026
Licence and permissions

Check for updates

Cite this: *Phys. Chem. Chem. Phys.*, 2026, **28**, 25615

Pushing the limits of NMR crystallography: a study on three forms of glycylglycine

Sean T. Holmes, *[ab] Aaron M. Viggiano,[c] Christine L. Plavchak, [c] Haylee R. Holman,[c] Megan M. Joyce, [c] Cameron S. Vojvodin,[ab] Xinsong Lin,[b] Robbie J. Iuliucci*[c] and Robert W. Schurko †[ab]

Received 28th June 2026,
Accepted 25th September 2026

DOI: 10.1039/d6cp02448c

rsc.li/pccp

NMR crystallography (NMRX), which integrates solid-state NMR (SSNMR) spectroscopy, X-ray diffraction (XRD), and density functional theory (DFT) calculations, provides deeper insight into crystal structures than any of these methods individually. With the goal of pushing the limits of NMRX, we have characterized three solid forms of the dipeptide glycylglycine, including a free base, a hydrochloride salt, and an unusual hemihydrochloride salt—the latter form is synthesized and characterized by single-crystal XRD here for the first time. SSNMR data include 2D ^{1}H–^{1}H DQ–SQ BABA spectra that are used to measure ^{1}H chemical shifts and provide assignments through homonuclear dipolar correlations, slow-spinning ^{1}H–^{13}C and ^{1}H–^{15}N CP/MAS spectra to determine the ^{13}C and ^{15}N chemical shift tensors, ultra-wideline ^{14}N WURST-CPMG spectra to measure the ^{14}N electric field gradient (EFG) tensors, 1D ^{35}Cl spectra to determine the ^{35}Cl EFG and chemical shift tensors, and 2D ^{35}Cl → ^{1}H D-RINEPT spectra to determine heteronuclear dipolar correlations between the chloride ions and nearby protons. Together with state-of-the-art DFT calculations, these parameters are related directly to molecular- and crystal-level structure and intermolecular hydrogen bonding. Modern DFT approaches using double-hybrid functionals are critical for predicting subtle differences in ^{13}C and ^{15}N chemical shift tensors between the three solid forms. By highlighting the current capabilities of NMRX, it is hoped that these results will open new avenues for the exploration of a plethora of materials and biosolids.

1. Introduction

NMR crystallography (NMRX) represents a powerful set of experimental and computational tools that leverage solid-state NMR (SSNMR) spectroscopy and computation to predict, validate, and refine crystal structures.[1–5] Commonly, NMRX features the combined use of SSNMR, X-ray diffraction (XRD), and computational methods (potentially including both *ab initio* and machine learning approaches) to obtain a more detailed understanding of molecular-level structure than is possible through any of these methods used in isolation.[6] In part, this comes about from the ability of NMRX to locate the positions of light atoms (in particular, hydrogen atoms) with a greater precision than XRD methods.[7–9] SSNMR and computational methods can provide insight into local structure when high quality single-crystal diffraction data are not available,[10–12] or can assist with determining crystal structures from Rietveld refinement of powder diffraction data.[13–17] It is also possible to combine SSNMR with crystal structure prediction (CSP) algorithms for the purpose of *de novo* structural determination (*i.e.*, NMRX-CSP).[18–22] More recent studies have demonstrated that it is even possible to obtain structures for amorphous solids,[23–25] an achievement that is largely outside the purview of diffraction methods.

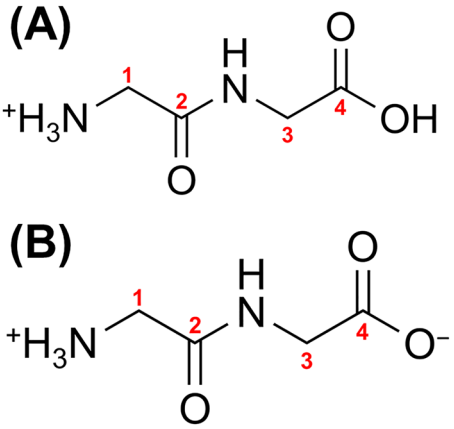
The power of NMRX stems from the ability of SSNMR to deliver site-specific chemical information with a level of detail unrivaled by any other spectroscopic, spectrometric, or microscopic technique. NMRX methods applied to organic solids often involve the measurement of dipole–dipole coupling constants, isotropic chemical shifts, and/or chemical shift tensors.[11] In addition, the quadrupolar interaction, which occurs for nuclides with nuclear spin quantum numbers $I > 1/2$, is highly sensitive to local electronic environments and weak, long-range interactions; as such, its inclusion, where possible, can further enhance NMRX studies, especially since all of these interactions have distinct physical origins.[10,26,27] Thus, NMRX benchmarking studies on important model compounds, especially those having a wide variety of NMR-active nuclides in diverse chemical environments, have far-reaching implications, helping to address fundamental questions in chemistry, materials science, and structural biology.

[a] *National High Magnetic Field Laboratory, Tallahassee, FL 32310, USA*
[b] *Department of Chemistry & Biochemistry, Florida State University, Tallahassee, FL 32306, USA. E-mail: sholmes2@fsu.edu*
[c] *Department of Chemistry, Washington and Jefferson College, Washington, PA 15301, USA. E-mail: riuliucci@washjeff.edu*
† Deceased February 2026.

Quantum chemical calculations using density functional theory (DFT) have advanced to the point where NMR interaction tensors can be predicted with high accuracy for many nuclides of elements across the periodic table. Such calculations are critical for SSNMR site assignment, as well as the interpretation of the relationships between chemical shift and electric field gradient (EFG) tensors with molecular-level structure and bonding. There are several necessary considerations for obtaining the best agreement between experimental and calculated values of NMR parameters for organic solids: (i) geometry optimizations on structural models obtained from diffraction or CSP techniques are essential and typically carried out using plane-wave DFT, which inherently incorporates intermolecular interactions;[28] (ii) for calculations of NMR interaction tensors, intermolecular interactions such as hydrogen bonding, which can strongly impact calculated values, are typically accounted for *via* periodic calculations using a plane-wave basis set,[29–31] or *via* cluster[32–34] or fragment-based[35–37] approaches that account for short-range lattice effects; (iii) when employing cluster-based approaches, electrostatic embedding can be used to better approximate the influences of the surrounding crystal lattice;[38–40] (iv) better accuracy can be obtained by using hybrid exchange correlation functionals (*e.g.*, B3LYP and PBE0), with the caveat that these methods are difficult to implement efficiently within the context of plane-wave DFT,[41] and therefore, are typically combined with more expensive cluster- or fragment-based structural models; and (v) if increased accuracy is desired, one can include a monomer correction, in which the NMR parameters of the central molecule of the cluster are predicted using a more expensive DFT method (*e.g.*, a double hybrid functional).[40,42–46]

The study of NMR interaction tensors in peptides (*e.g.*, ^{13}C and ^{15}N chemical shift tensors, ^{13}C–^{15}N dipolar coupling constants, *etc.*) has provided valuable insights into the relationships between SSNMR spectra and local structure in these important compounds. In part, research on the characterization of crystalline peptides and related model systems has attracted considerable interest, since they provide insight into the behaviors of amino acids in proteins and biosolids.[47,48] For example, Stark *et al.* and Harbison *et al.* used multinuclear SSNMR approaches to study isotopically-enriched single crystals of [1-^{13}C]glycyl[^{15}N]glycine HCl·H_2O.[49,50] Similarly, Takeda *et al.* measured the ^{13}C chemical shift tensors of the carbonyl moieties (selectively labelled in ^{13}C) for three forms of glycylglycine using single-crystal NMR.[51] The body of literature on measurement and calculation of ^{13}C and ^{15}N chemical shift tensors in amino acids, peptides, and proteins highlights their relationships to crystal structure and potential use in NMRX applications,[52–65] including the *de novo* determination of peptide crystal structures.[66,67]

Here, we report the structural characterization of three solid forms of the dipeptide glycylglycine using multinuclear and multidimensional SSNMR spectroscopy, single-crystal X-ray diffraction, and DFT calculations (Scheme 1). We first discuss the synthesis of the novel salt glycylglycine hemihydrochloride (**GG–1/2HCl**) and the determination of its crystal structure *via* single-crystal X-ray diffraction (SCXRD), in which the glycylglycine molecules are found to dimerize through a short, single-well hydrogen bond. The structure of this unique solid form is contrasted with the previously-reported glycylglycine monohydrochloride monohydrate (**GG–HCl–H_2O**)[68] and the α polymorph of the zwitterionic free base form of glycylglycine (**GG**).[69] We then explore the characterization of each form by multinuclear SSNMR spectroscopy, making use of all accessible naturally-occurring isotopes, including ^{1}H, ^{13}C, ^{14}N, ^{15}N, and ^{35}Cl (N.B.: ^{17}O SSNMR could be a future avenue of exploration that would require robust synthetic methodologies to isotopically label the peptides).[70,71] The experimentally-determined chemical shift and EFG tensors are compared with those derived from DFT calculations to elucidate their relationships to structure and bonding, with particular attention given to the computational protocols that yield the best agreement between experiment and theory. Finally, we discuss how this NMRX approach, which combines multinuclear SSNMR spectroscopy, single-crystal XRD, and state-of-the-art DFT methods, can be applied as a powerful and reliable protocol for the precise structural characterization of materials and biosolids.



Scheme 1 The molecular structure of glycylglycine in (A) its charged form and (B) its zwitterionic form. The numbering of the carbon atoms is shown in red.

2. Experimental and computational details

2.1 Samples

Samples of **GG** and **GG–HCl–H_2O** were purchased from MilliporeSigma and used without further purification. The synthesis of **GG–1/2HCl** is described in Section 3.1. To verify the purities of the samples, PXRD patterns were acquired using a Rigaku MiniFlex benchtop diffractometer with a Cu K_α radiation source and a D/teX Ultra2 detector. Samples were packed on zero-background silicon wafers with a well size of 5.0 × 0.2 mm. Experiments were conducted with an X-ray voltage of 40 kV, a current of 20 mA, 2θ angles over the range of 5–50°, a step size of 0.03°, and a dwell time of 5 s. PXRD patterns match simulated patterns based on their known crystal structures (Fig. S1). No impurity phases are indicated.

 This journal is © the Owner Societies 2026

2.2 Single-crystal X-ray diffraction

A single clear block-shaped crystal of **GG–1/2HCl** with approximate dimension 0.578 × 0.429 × 0.21 mm^3 was adhered to a Mitegen loop with Paratone oil. Crystallographic data were collected at temperature 150 K on a Rigaku-Oxford Diffraction XtaLAB-Synergy-S diffractometer with a Hypix-6000HE detector, using Cu *K*α radiation of wavelength 1.54187 Å. The intensity data were measured by a ω-scan with 0.5° oscillations for each frame with the intensity that is more than 10 : 1 for data-to-parameter ratio. CrysAlis^{Pro} was used for data collection, absorption correction, and data reduction. The structures were solved with the dual-space algorithm using SHELXT[72] and refined by full-matrix least-squares methods on F^2 with SHELXL-2014[73] using the GUI Olex2.[74] All non-hydrogen atoms were refined anisotropically. Hydrogen atoms were inserted at calculated positions or, if possible, based on difference Fourier analysis and refined with a riding model or without restrictions.

2.3 Solid state nuclear magnetic resonance spectroscopy

2.3.1 Overview. SSNMR spectra at 9.4 T were acquired at Washington & Jefferson College (Washington, PA) using a 9.4 T Oxford wide bore magnet, a Varian INOVA console, and a 7.5 mm Varian T3 HX MAS probe with samples packed into 7.5 mm o.d. pencil-style zirconia rotors. The relevant Larmor frequencies were $\nu_0(^1H)$ = 399.81 MHz and $\nu_0(^{15}N)$ = 40.52 MHz. Spectra at 14.1 T were collected at the National High Magnetic Field Laboratory (NHMFL, Tallahassee, FL) using an Oxford wide-bore magnet, a Bruker Avance NEO console, and a NHMFL-built 5.0 mm low-E HX static probe with samples packed in 5.0 mm o.d. polychlorotrifluoroethylene (PCTFE) sample containers. The relevant Larmor frequencies were $\nu_0(^1H)$ = 600.07 MHz and $\nu_0(^{35}Cl)$ = 58.78 MHz. At 18.8 T, data were acquired at the NHMFL using an Oxford medium-bore magnet, a Bruker Avance NEO console, a Bruker 1.3 mm HCN MAS probe (with the ^{15}N channel tuned to ^{35}Cl) with samples packed into a 1.3 mm o.d. Bruker-style rotor, a NHMFL-built 3.2 mm low-E HXY MAS probe with sample packed in 3.2 mm o.d. pencil-style zirconia rotors, or a NHMFL-built 5.0 mm low-E HX static probe with samples packed in 5.0 mm o.d. PCTFE sample containers. The relevant Larmor frequencies were $\nu_0(^1H)$ = 800.12 MHz, $\nu_0(^{13}C)$ = 201.22 MHz, $\nu_0(^{14}N)$ = 57.80 MHz, and $\nu_0(^{35}Cl)$ = 78.39 MHz. All acquisition parameters are provided in Tables S1–S7. Spectra were processed using Bruker Topspin 4.1.4 and fit using ssNake 1.3 or 1.4.[75] Pulse sequences and recommended calibration parameters and standards are available at https://github.com/rschurko.

2.3.2 2D ^{1}H–^{1}H spectra. 2D ^{1}H–^{1}H DQ–SQ spectra were acquired at 18.8 T using a MAS frequency of ν_{rot} = 50 kHz, π/2 pulse widths of 2.5 μs, and optimized relaxation delays of 2–30 s, one rotor period of back-to-back (BABA) recoupling,[76,77] 128 t_1 increments, and 4 or 32 coadded transients per increment. ^{1}H rf amplitudes were calibrated through separate ^{1}H π/2 pulse-spin lock pulse experiments.[78] Additional 1D spectra were acquired using a Hahn echo sequence. ^{1}H chemical shifts were referenced to neat TMS at $\delta_{iso}(^1H)$ = 0.0 ppm using the high-frequency peak in solid L-histidine HCl·H_2O at $\delta_{iso}(^1H)$ = 17.2 ppm as a secondary ref. 79.

2.3.3 ^{13}C spectra. ^{13}C spectra were acquired at 18.8 T using a variable-amplitude CP/MAS sequence with a spinning rate of ν_{rot} = 2.8 kHz.[80–84] Data were acquired using a 3.33 μs ^{1}H π/2 pulse, a ramped-amplitude Hartmann–Hahn matching field of $\nu_2(^1H)$ = 50 kHz (matched on the X channel),[85] a contact time of 3.0 ms, and a SPINAL-64 ^{1}H decoupling field of $\nu_2(^1H)$ = 75 kHz.[86] ^{13}C chemical shifts were referenced to neat TMS at δ_{iso} = 0 ppm using the high-frequency peak of ^{13}C-labeled α-glycine at 176.5 ppm as a secondary ref. 87 and 88.

2.3.4 ^{15}N spectra. Natural-abundance ^{15}N spectra were acquired at 9.4 T using a variable-amplitude CP/MAS sequence with a spinning rate of ν_{rot} = 900 or 1450 Hz.[80–84] Data were acquired using a 3.85–4.7 μs ^{1}H π/2 pulse, a ramped-amplitude Hartmann–Hahn matching field of $\nu_2(^1H)$ = 26.5–32.5 kHz (matched on the X channel),[85] a contact time of 1.0 ms, and a SPINAL-64 ^{1}H decoupling field of $\nu_2(^1H)$ = 53–65 kHz.[86] ^{15}N chemical shifts were referenced to neat ammonia at δ_{iso} = 0 ppm using the high-frequency peak of ^{15}N-labeled α-glycine at 33.4 ppm as a secondary ref. 89 and 90.

2.3.5 ^{14}N spectra. Ultra-wideline $^{14}N\{^1H\}$ spectra were obtained using the WURST-CPMG pulse sequence.[91–94] The experiments utilized 50 μs WURST-80 pulses with a maximum rf amplitude of $\nu_1(^{14}N)$ = 25 kHz that were swept linearly from low to high frequency, covering a total sweep width of 1.0 MHz. A continuous wave (cw) decoupling field of $\nu_2(^1H)$ = 50 kHz was applied for the duration of each scan. Only the high-frequency sides of the ^{14}N powder patterns were collected; the low-frequency sides of the patterns were produced by reflection, as discussed previously.[95,96] Due to the breadths of the patterns, individual sub-spectra were acquired using evenly spaced transmitter frequencies at an integer multiple of the spikelet separation (*ca.* 100 kHz).[97,98] Sub-spectra were processed through Fourier transformation of their respective FIDs, and subsequent coaddition of the resulting spectra in the frequency domain. ^{14}N chemical shifts were referenced externally to neat ammonia using NH_4Cl as a secondary reference, although these values are not reported due to their inherent uncertainties.

2.3.6 ^{35}Cl spectra. $^{35}Cl\{^1H\}$ spectra were acquired at 14.1 T and 18.8 T using different pulse sequences, depending on the nature of the SSNMR powder pattern. The majority of spectra were acquired using a Hahn-echo or rotor-synchronized Hahn-echo sequence with central-transition (CT, +1/2 ↔ −1/2)-selective π/2 pulses.[99] A ^{1}H cw decoupling field was applied in all experiments. The static spectrum of **GG–1/2HCl** acquired at 14.1 T was obtained using the WURST-CPMG sequence.[91,92] The MAS spectrum for **GG–1/2HCl** acquired at 18.8 T and ν_{rot} = 50 kHz achieved pre-polarization through blocks of WURST-80 pulses applied on the ^{35}Cl channel, using a 38.0 μs pulse width (followed by a 2.0 μs delay), a maximum rf of 50 kHz, a 50 kHz sweep width, and an optimized transmitter offset of 400 kHz.[100,101] ^{35}Cl chemical shifts were referenced to 0.1 M NaCl(aq) at $\delta_{iso}(^{35}Cl)$ = 0 ppm.[102]

2.3.7 ^{35}Cl → ^{1}H D-RINEPT spectra. 2D ^{35}Cl → ^{1}H spectra were obtained at 18.8 T using the dipolar-refocused insensitive

nuclei enhanced by polarization transfer (D-RINEPT) sequence.[103,104] These spectra were acquired using a spinning rate of ν_{rot} = 50 kHz, a recycle delay of 0.5 s, 128 t_1 increments, and 512 scans per increment. A 5.0 μs CT-selective π/2 pulse was applied on the ^{35}Cl channel. Rotor-synchronized dipolar recoupling was applied on the ^{1}H channel using symmetry-based $SR4_2^1$ recoupling.[105] The rf field was set to two times ν_{rot} (*i.e.*, 100 kHz) to fulfill the second-order R^3 condition. Pre-polarization was achieved through pulse blocks applied on the ^{35}Cl channel prior to the D-RINEPT transfer step, using WURST-80 pulses with a 38.0 μs duration (followed by a 2.0 μs delay), a maximum rf of 30 kHz, a 50 kHz sweep width, and optimized transmitter offsets ranging between 400–500 kHz.[100,101]

2.4 Quantum chemical computations

2.4.1 Geometry optimizations. Plane-wave DFT geometry optimizations were performed using the CASTEP module within BIOVIA Materials Studio 2020.[106] Experimental crystallographic data from single-crystal X-ray diffraction studies (either previous studies[68,69] or the data reported herein) were used as initial structural models. Calculations used the RPBE functional,[107] ultrasoft pseudopotentials generated on-the-fly,[108] a plane-wave cutoff energy of 800 eV, and a *k*-point spacing of 0.05 Å^{-1}.[109] Structural refinements employed the LBFGS energy-minimizing scheme,[110] with convergence thresholds including a maximum change in energy of 5×10^{-6} eV atom^{-1}, a maximum displacement of 5×10^{-4} Å atom^{-1}, and a maximum Cartesian force of 10^{-2} eV Å^{-1}. Semi-empirical dispersion corrections were introduced using the two-body dispersion force field model of Grimme (DFT-D2),[111,112] or a reparametrized version of this method introduced by the authors for applications in NMR crystallography (DFT-D2*).[113–115] These calculations used a three-step geometry optimization in which (i) hydrogen atoms were first relaxed at the RPBE-D2 level (s_6 = 1.0; d = 20.0); (ii) all atoms were relaxed at the RPBE-D2 level; and (iii) atoms involved in intermolecular hydrogen bonds were relaxed at the RPBE-D2* level (s_6 = 1.0; d = 3.5). These refined crystal structures were used in all subsequent computational analyses.

2.4.2 Single-point energy calculations. Single-point energy calculations were performed on a dimer of the novel solid form **GG–1/2HCl**, following plane-wave DFT geometry optimization. These calculations used the double-hybrid functional B2PLYP[116] because of its demonstrated accuracy on modelling thermochemistry and noncovalent interactions.[117] This was combined with the TZ2P basis set, along with Grimme's three-body dispersion force field with Becke–Johnson damping, *i.e.*, D3(BJ).[118]

2.4.3 Magnetic shielding and EFG tensors. ^{14}N and ^{35}Cl EFG tensors, as well as ^{35}Cl magnetic shielding tensors, were calculated within CASTEP using the same parameters and approximations as those in the geometry optimizations,[31] with the latter calculations employing the GIPAW method.[30,119,120]

^{1}H, ^{13}C, and ^{15}N magnetic shielding tensors were calculated using the Amsterdam density functional (ADF) program included in the AMS suite (AMS 2021.106).[121] These latter calculations used structural models comprising a large cluster of up to fifteen molecules and the appropriate number of chloride ions, as discussed previously.[32–34,40] Magnetic shielding tensors were computed using the GIAO method.[76,77] These calculations used the hybrid functional PBE0.[122] Relativistic effects were implemented through the zeroth-order regular approximation (ZORA) Hamiltonian, as expanded to include scalar terms.[123] A basis set partitioning scheme was applied in which the central molecule within the cluster was assigned the Slater-type TZ2P basis set with Becke integration set to ''excellent'',[124,125] whereas all other molecules in the cluster were assigned the DZP basis set with ''normal'' Becke integration. A linear-dependence threshold of 10^{-4} was applied. Magnetic shielding and EFG tensors are calculated only for the central molecule within the cluster. Electrostatic embedding of the clusters is accomplished through the conductor-like screening model (COSMO).[126–130] Water was selected as the solvent, using Delley-type cavity construction,[131] with atomic cavity radii based on the van der Waals radii of Allinger.[132]

Calculations employing the monomer correction used both the ADF and ORCA 6.0.1[133] software packages. The ADF calculations employed or the PBE0 functional[122] and the same parameters and approximations described above. The ORCA calculations used the GIAO method,[134,135] along with the double-hybrid functional PBE0-DH,[136] and the Gaussian-type segmented-contracted basis set pcSseg-3.[137] For the PBE0-DH calculations, the RIJCOSX-MP2 approximation was used,[138] along with the and the RI-MP2 auxiliary basis set cc-pwCVTZ.[139] The magnetic shielding tensors were obtained from the results of three separate types of calculations: (i) a calculation in ADF using the molecular cluster (with COSMO electrostatic embedding) as the structural model, as described above; (ii) a calculation in ADF using an isolated molecule as the structural model; and (iii) a calculation in ORCA using an isolated molecule as the structural model. Calculations (i) and (ii) provide the intermolecular contributions to the ^{1}H, ^{13}C, and ^{15}N magnetic shielding tensors at the hybrid DFT level, whereas calculation (iii) is a high-level monomer correction (using a double-hybrid method) to the magnetic shielding tensors, where the three contributions are coadded, and the resulting tensor is diagonalized to yield the principal components.[40,42–45]

3. Results and discussion

3.1 Synthesis and crystal structure of GG–1/2HCl

Crystals of **GG–1/2HCl** were prepared by dissolving **GG** and 12 M HCl in a 2 : 1 molar ratio using the minimum amount of water and gentle heating, followed by slow evaporation of the solution. This mixture was then diluted with ethanol (2 : 1 v/v ethanol : mixture) and left to sit for two weeks until large crystals were obtained. Analysis by ^{15}N SSNMR revealed a novel crystalline phase of glycylglycine with chemical shifts distinct from those of **GG** and **GG–HCl–H_2O**. When these synthetic protocols are not followed, the result is a mixture of phases, as indicated by ^{15}N SSNMR. When the mixture is not diluted in ethanol, the resulting product is a mixture of **GG–1/2HCl** and **GG–HCl–H_2O**. When an excess of **GG** is used (relative to HCl), an additional **GG** impurity is evident. When excess **GG** and an

 This journal is © the Owner Societies 2026

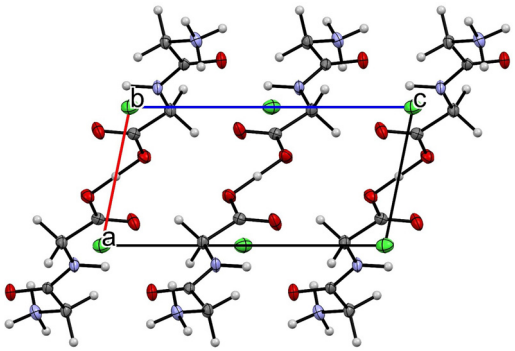


Fig. 1 The structure of glycylglycine hemihydrochloride (**GG–1/2HCl**), as determined by single-crystal X-ray diffraction. The O–H bond length is 1.198 Å, the O–O distance is 2.3964 Å, and the O···H···O bond angle is 180°.

insufficient volume of ethanol are used, mixtures of all three phases are observed.

Suitable single crystals of **GG–1/2HCl** were analyzed using SCXRD (Fig. 1). **GG–1/2HCl** crystallizes in the monoclinic $P2_1/c$ space group with $Z = 2$ and $Z' = 0.5$, with the unit cell parameters: $a = 4.5861$ Å, $b = 15.6670$ Å, $c = 9.1663$ Å, $\beta = 101.487°$, and $V = 645.411$ Å^3 (Table 1). The molecular-level structure consists of dimerized glycylglycine molecules that share a single hydrogen atom between them (r(O···H) = 1.198 Å, r(O···O) = 2.3964 Å, and ∠(O···H···O) = 180° in the geometry optimized crystal structure). The asymmetric unit contains one glycylglycine molecule, with the complete dimer generated by a crystallographic inversion center passing through the O···H···O bridge. This constrains the hydrogen atom to the midpoint between the oxygen atoms, resulting in a symmetric, single-well hydrogen bond. The chloride ions also reside at inversion centers. The crystal structure is available from the Cambridge Structural Database under deposition number 2535045.

To further validate the position of the hydrogen atom within the O···H···O bridge, a series of single-point energy calculations were carried out in which the hydrogen atom was moved away from the center of the dimer toward one of the oxygen atoms, without application of symmetry constraints. In short, these calculations establish that the energy landscape of the O···H···O bond consists of a single symmetric well, with its minimum corresponding to the state in which both O···H bond lengths are identical (*i.e.*, when the hydrogen resides exactly between the two oxygen atoms). These results are shown in Fig. 2.

3.2 Solid-state NMR

3.2.1 ^{1}H–^{1}H DQ–SQ spectra. 2D ^{1}H–^{1}H DQ–SQ (double quantum–single quantum) spectra were acquired (18.8 T; ν_{rot} = 50 kHz) using one rotor period of BABA recoupling (Fig. 3). In BABA DQ–SQ experiments, the ^{1}H–^{1}H homonuclear dipolar coupling is recoupled during the DQ excitation and reconversion periods, leading to the observation of correlations between ^{1}H spins. Due to the short recoupling period of one rotor cycle, off-diagonal peaks in the 2D spectrum correspond only to the most strongly coupled sites, whereas peaks appearing along the $\delta_{DQ} = 2\delta_{SQ}$ diagonal arise from crystallographically equivalent protons that are close enough to one another to have through-space dipolar correlations and/or proximate protons with similar chemical shifts. The former manifest as pairs of peaks that are equidistant from the diagonal line with a value of δ_{DQ} equal to the sum of the two distinct values of δ_{SQ}, *i.e.*, $\delta_{DQ} = \delta_{SQ}^{(1)} + \delta_{SQ}^{(2)}$.

The ^{1}H chemical shifts for most sites in each material were determined and assigned with these spectra and DFT calculations (Table 2 and Fig. S3), with the only exception being **GG**, for which only two of the four ^{1}H species are resolved (*i.e.*, the two ethylenic protons have undifferentiable chemical shifts, as do the amine and amide protons). We note the very deshielded ^{1}H of the carboxylic acid moiety of **GG–1/2HCl** at $\delta_{iso}(^1H)$ = 19.3 ppm, which is reflective of its unusual chemical bonding environment as part of a single-well hydrogen bond. In contrast, the carboxylic acid resonance for **GG–HCl–H$_2$O** appears at a more typical value of $\delta_{iso}(^1H)$ = 12.4 ppm, while no corresponding signal occurs for the zwitterionic form of **GG**. All other ^{1}H chemical shifts fall within the anticipated ranges for their respective moieties.

Because of the importance of the hydrogen atoms and relevant hydrogen bonding interactions associated with hydroxyl group (R–OH) and O···H···O configurations in organic solids, a few comments are provided on the interpretation of these spectra. For **GG–HCl–H$_2$O**, a diagonal peak is observed at $\delta_{iso}(^1H)$ = 12.4 ppm because there is an intermolecular

Table 1 Crystal data and structure refinement for glycylglycine hemihydrochloride (**GG–1/2HCl**)

Identification code	**GG–1/2HCl**	ρ_{calc} (g cm^{-3})	1.547
Empirical formula	$C_8H_{17}ClN_4O_6$	μ (mm^{-1})	2.94
Formula weight	300.7	F(000)	316
Temperature/K	150.0(1)	Crystal size (mm^3)	0.578 × 0.429 × 0.21
Crystal system	Monoclinic	Radiation	Cu $K\alpha$ (λ = 1.54184)
Space group	$P2_1/c$	2θ range for data collection (°)	11.296 to 152.942
a/Å	4.58606(10)	Index ranges	$-5 \le h \le 5$, $-19 \le k \le 12$, $-10 \le l \le 11$
b/Å	15.6670(4)	Reflections collected	4463
c/Å	9.16633(19)	Independent reflections	1248 [R_{int} = 0.0379, R_{sigma} = 0.0331]
α/°	90	Data/restraints/parameters	1248/0/91
β/°	101.487(2)	Goodness-of-fit on F^2	1.052
γ/°	90	Final R indexes [$I \ge 2\sigma(I)$]	R_1 = 0.0397, wR_2 = 0.1112
Volume/Å^3	645.41(3)	Final R indexes [all data]	R_1 = 0.0420, wR_2 = 0.1143
Z, Z'	2, 0.5	Largest diff. peak/hole (e Å^{-3})	0.41/−0.37

Uncertainties in the last digit(s) are indicated in parentheses (*e.g.*, 15.6670(4) = 15.6670 ± 0.0004).

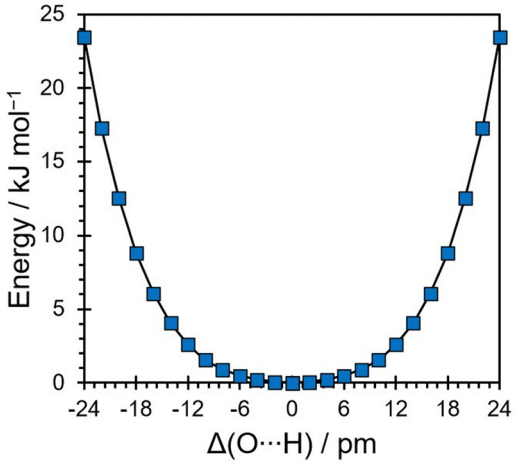


Fig. 2 DFT calculations of the difference in energy of the **GG–1/2HCl** dimer as the hydrogen atom is moved closer to one of the oxygen atoms within the O···H···O bridge. Calculations are performed at the B2PLYP-D3(BJ) level.

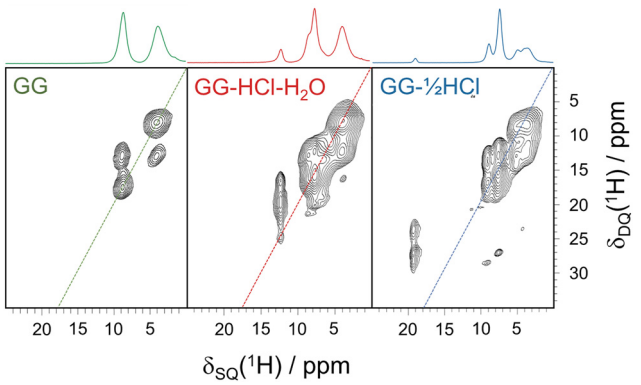


Fig. 3 2D ^{1}H–^{1}H DQ–SQ spectra acquired at 18.8 T using a MAS frequency of ν_{rot} = 50 kHz and one rotor period of BABA recoupling. The upper traces result from separate 1D ^{1}H Hahn echo experiments.

Table 2 Experimental and calculated ^{1}H chemical shifts[a,b,c]

		Exp. shift (ppm)	Calc. shift (ppm)
GG	Ethylene (C1)	4.0(3)	5.2
	Ethylene (C3)	4.0(3)	5.2
	Amine	8.7(2)	7.4
	Amide	8.7(2)	7.5
GG–HCl–H$_2$O	Ethylene (C1)	4.0(2)	5.5
	Ethylene (C3)	3.9(2)	5.0
	Water	6.6(1)	5.6
	Amine	7.7(1)	6.7
	Amide	8.6(1)	7.4
	Carboxylic acid	12.4(2)	11.4
GG–1/2HCl	Ethylene (C1)	5.1(2)	5.7
	Ethylene (C3)	4.4(2)	5.4
	Amine	7.6(1)	6.5
	Amide	9.1(1)	7.5
	Carboxylic acid	19.3(1)	22.1

[a] Uncertainties in the last digit of the experimental chemical shifts (indicated in parentheses) are estimated based on factors such as ^{1}H peak widths and the extent of overlap between peaks. [b] Theoretical ^{1}H chemical shift tensors were obtained from DFT calculations on geometry optimized structures, performed at the PBE0-DH level in ORCA and ADF. [c] Additional details are provided in the SI (Fig. S3).

interaction between R–OH protons, which are separated by *ca.* 3.7 Å. Other intermolecular correlations are also observed, including with the ethylenic C3 (r(H–H) = 2.8 Å) and amine (r(H–H) = 3.1 Å) protons. Interestingly, no correlation is observed between the R–OH (12.4 ppm) and H_2O protons (6.6 ppm); this suggests that the motions of the H_2O molecules are rapid compared to the timescale of the NMR experiment (*i.e.*, they are in the fast motion limit). For **GG–1/2HCl**, no diagonal peak is observed for the O···H···O protons at δ_{iso}(^{1}H) = 19.3 ppm because the nearest proton of the same type is located at a distance of *ca.* 9.1 Å. However, intermolecular interactions between O···H···O protons and nearby amine (r(H–H) = 2.8 Å) and amide (r(H–H) = 3.8 Å) protons, as well as an intramolecular interaction with the ethylenic C3 protons (r(H–H) = 3.8 Å), are evident in the spectrum. See Fig. S4 for the spectrum of **GG–1/2HCl** with a wider spectral window.

3.2.2 ^{13}C spectra. Careful consideration of experimental conditions is necessary for acquiring high quality ^{1}H–^{13}C CP/MAS SSNMR spectra to extract reliable ^{13}C chemical shift tensor parameters. Optimal Hartmann–Hahn matching conditions were established over a MAS frequency range from ν_{rot} = 2.5 to 10.0 kHz. The isotropic chemical shifts were determined with ν_{rot} = 10 kHz. For the measurement of the chemical shift tensors, a slower spinning rate of ν_{rot} = 2.8 kHz was selected to ensure the observation of at least three pairs of sidebands for the ethylene peaks, while also minimizing overlap between isotropic peaks and spinning sidebands.

Each ^{13}C spectrum features four isotropic peaks, which is consistent with the crystal structures (Fig. 4). There are no impurity phases observed in any of the spectra, with no noticeable splitting in the ^{13}C peaks. The principal components of the ^{13}C chemical shift tensors were obtained from analysis of the relative intensities of the spinning sideband manifold through numerical simulations using ssNake (Fig. S4–S6).[75] Peaks in the difference spectra are nonetheless more intense than the surrounding noise, suggesting that ^{14}N–^{13}C residual dipolar coupling may affect the appearances of the patterns to some degree, even at 18.8 T.

Among the ^{13}C chemical shift tensors (Table 3), the most pronounced differences between the three solid forms occur for the carbonyl carbons (C4), where δ_{iso}(^{13}C) values vary little, but Ω and κ differ markedly. The value of Ω is smallest for **GG** (129.0 ppm), intermediate for **GG–1/2HCl** (135.8 ppm), and largest for **GG–HCl–H$_2$O** (151.0 ppm), whereas the values of κ are similar for **GG** and **GG–1/2HCl** (0.02 and 0.03, respectively), but substantially different for **GG–HCl–H$_2$O** (−0.48 ppm). The distinct κ in **GG–HCl–H$_2$O** results from its value of δ_{22} (147.0 ppm), which differs from those of **GG** and **GG–1/2HCl** (174.4 and 177.6 ppm, respectively). Similar variations are also observed for the ethylenic carbons (C3), especially in terms of the skews (κ = 0.07 for **GG–HCl–H$_2$O**, and κ = 0.87 and 0.72 for **GG** and **GG–1/2HCl**, respectively). In contrast, there is comparatively little variation in the chemical shift tensors for amide

 This journal is © the Owner Societies 2026

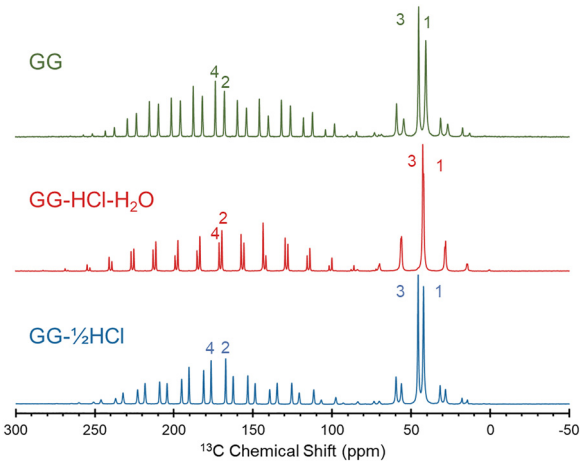


Fig. 4 $^{1}H-^{13}C$ CP/MAS spectra acquired at 18.8 T using a spinning rate of ν_{rot} = 2.8 kHz.

carbons (C1) and second ethylenic carbons (C2) because the local structural differences are comparatively minor.

Because the largest variations in chemical shift tensors are observed for C4 and C3, it is probable that these differences reflect the protonation states of the glycylglycine molecules, differences in hydrogen bonding arrangements, and any number of subtle variations in bond lengths and angles among each solid form. In carboxylic acids and carboxylates such as C4, the principal components of the chemical shift tensors have well-known orientations, where δ_{22} is oriented along or near the C═O bonding axis, δ_{11} is perpendicular to this axis and within the plane of the functional group, and δ_{33} is perpendicular to the functional group; as a result, δ_{11} and δ_{22} are highly reflective of differences and/or changes in hydrogen bonding.[62] Consistent with these previous observations, we see here that there is very little variation in δ_{33} between the three solid forms of glycylglycine, whereas the variation in δ_{11} and δ_{22} is significant.

Table 4 ^{13}C chemical shift tensor metrics to differentiate between COOH and COO^- moieties, as well as the measured values for the three solid forms of glycylglycine

Metric	COOH	COO^-	GG	GG–HCl–H_2O	GG–1/2HCl
δ_{11}	>250	<250	237.7	259.0	243.8
$\delta_{11} + (\delta_{33} - \delta_{22})$	>185	<185	172.0	220.0	174.2
$\delta_{11} - \delta_{22}$	>73	<73	63.3	112.0	66.2

^{13}C chemical shift tensors can also be used to differentiate between COOH and COO^- moieties in the absence of a well-resolved structure;[131,140] in light of this, it is interesting to determine whether the values determined here for **GG–1/2HCl** cluster more with one functional group or the other, or if they are more consistent with some intermediate state. Gu and McDermott proposed the following metrics to differentiate between COOH and COO^- moieties: (i) $\delta_{11} > 250$ ppm for COOH and <250 ppm for COO^-; (ii) $\delta_{11} + (\delta_{33} - \delta_{22}) > 180$ ppm for COOH and <180 ppm for COO^-; and (iii) $\delta_{11} - \delta_{22} > 73$ ppm for COOH and <73 ppm for COO^-.[64] According to these metrics, the ^{13}C chemical shift tensor for **GG–1/2HCl** clusters with those of COO^- groups (Table 4), meaning that the

Table 3 Experimental and calculated ^{13}C chemical shift tensors[a,b,c,d]

			δ_{11} (ppm)	δ_{22} (ppm)	δ_{33} (ppm)	δ_{iso} (ppm)	Ω (ppm)	κ	d_ν (ppm)
GG	C1	Exp.	55.8	45.8	20.2	40.6	35.6	0.44	—
		Calc.	55.6	44.1	22.2	40.6	33.4	0.31	0.9
	C2	Exp.	239.3	176.3	88.0	167.9	151.3	0.17	—
		Calc.	241.5	173.0	87.6	167.4	153.9	0.11	1.5
	C3	Exp.	57.3	55.1	22.9	45.1	34.4	0.87	—
		Calc.	63.9	53.8	22.7	46.8	41.2	0.51	2.8
	C4	Exp.	237.7	174.4	108.7	173.6	129.0	0.02	—
		Calc.	241.7	175.2	104.6	173.8	137.1	0.03	2.1
GG–HCl–H_2O	C1	Exp.	57.4	49.0	21.5	42.6	35.9	0.53	—
		Calc.	57.7	46.1	23.5	42.4	34.2	0.32	1.3
	C2	Exp.	242.9	177.9	87.9	169.6	155.0	0.16	—
		Calc.	245.0	179.3	85.8	170.0	159.2	0.17	1.3
	C3	Exp.	67.2	43.1	15.6	42.0	51.6	0.07	—
		Calc.	71.7	43.2	16.8	43.9	54.9	−0.04	2.3
	C4	Exp.	259.0	147.0	108.0	171.3	151.0	−0.48	—
		Calc.	260.8	144.6	106.1	170.5	154.7	−0.50	1.5
GG–1/2HCl	C1	Exp.	56.4	47.1	23.1	42.2	33.3	0.44	—
		Calc.	59.7	44.2	27.3	43.7	32.4	0.04	2.5
	C2	Exp.	238.4	172.2	91.2	167.3	147.2	0.10	—
		Calc.	243.9	169.2	86.6	166.6	157.3	0.05	2.9
	C3	Exp.	58.8	53.9	24.2	45.6	34.6	0.72	—
		Calc.	64.8	51.7	20.4	45.6	44.4	0.41	2.7
	C4	Exp.	243.8	177.6	108.0	176.5	135.8	0.03	—
		Calc.	250.5	177.6	102.9	177.0	147.6	0.01	3.1

[a] Calculated ^{13}C chemical shift tensors were obtained from DFT calculations on geometry optimized structures, performed at the PBE0-DH level in ORCA and ADF. [b] The principal components of the chemical shift tensors are defined using the frequency-ordered convention such that $\delta_{11} \geq \delta_{22} \geq \delta_{33}$. The isotropic chemical shift, span, and skew are given by $\delta_{iso} = (\delta_{11} + \delta_{22} + \delta_{33})/3$, $\Omega = \delta_{11} - \delta_{33}$, and $\kappa = 3(\delta_{22} - \delta_{iso})/\Omega$, respectively. [c] The chemical shift distance, d_ν, describes the agreement between experimental and calculated chemical shift tensors, as described in the SI (S1). [d] Uncertainties in each principal component are estimated to be ±1.0 ppm, based on bidirectional variation of Ω and κ.

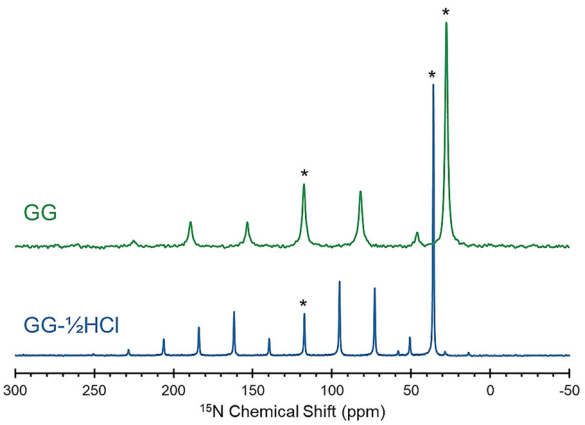


Fig. 5 ^{1}H–^{15}N CP/MAS spectra acquired at 9.4 T using a spinning rate of ν_{rot} = 900 Hz or 1450 Hz. Isotropic peaks are indicated by asterisks.

O···H···O interactions are more similar to hydrogen bonds than to covalent bonds. Furthermore, a recent study by Toomey *et al.*[9] showed that the metric $\delta_{11} - \delta_{22}$ is directly proportional to the R–O···H hydrogen bond length, *i.e.*, $r(\mathrm{O}\cdots\mathrm{H}) = 0.026 \times (\delta_{11} - \delta_{22}) - 0.385$ Å. Based on this equation and the value of $\delta_{11} - \delta_{22}$ = 66.2 ppm for **GG–1/2HCl**, one would expect a hydrogen bond length of 1.34 Å, with an anticipated uncertainty of ±0.09 Å. This is very similar to the 1.22 Å determined herein by SCXRD and subsequent refinement by plane-wave DFT calculations. This good agreement is especially noteworthy, because the previous work did not consider R–O···H hydrogen bond lengths below *ca.* 1.6 Å.

3.2.3 ^{15}N and ^{14}N spectra. Nitrogen has two NMR-active isotopes: ^{15}N (I = 1/2; n.a. = 0.365%) and ^{14}N (I = 1; n.a. = 99.6%). ^{15}N spectra are often acquired by the ^{1}H–^{15}N CP/MAS methods, yielding relatively sharp peaks similar to those in ^{1}H–^{13}C CP/MAS spectra, but often face long experiment times due to the low natural abundance of ^{15}N. ^{14}N spectra can be acquired using both direct- and indirect-excitation techniques:[141,142] the former typically employ frequency-swept pulses for broadband excitation, refocusing, and/or polarization transfer; CPMG loops for signal gain proportional to $T_2^{\mathrm{eff}}(^{14}\mathrm{N})$; and in cases of powder patterns ranging from hundreds of kHz to several MHz in breadth, transmitter stepping to achieve relatively distortionless powder patterns of high uniformity. Together, ^{15}N and ^{14}N spectra provide rich information on nitrogen chemical shift and EFG tensors.

We first discuss the ^{15}N spectra acquired using ^{1}H–^{15}N CP/MAS techniques under slow MAS conditions. The ^{15}N chemical shift tensors for **GG–HCl–H$_2$O** were previously measured using ^{15}N SSNMR at natural abundance on a microcrystalline powder sample,[58] and for a ^{15}N-labelled single crystal of [1-^{13}C]glycyl[^{15}N]glycine HCl·H$_2$O;[50] hence, these are not explored further in the present study. Herein, ^{15}N spectra for **GG** and **GG–1/2HCl** (Fig. 5) were acquired using spinning rates of ν_{rot} = 1450 and 900 Hz, respectively, whereas as a spectrum for **GG** was also acquired under static conditions to obtain data for the amine site (Fig. S7 and S8). The principal components of the ^{15}N chemical shift tensors were obtained from an analysis similar to that of the ^{13}C data (*vide supra*), except for those of **GG**, which were obtained by simultaneously fitting static and MAS spectra.

The ^{1}H–^{15}N CP/MAS spectra of **GG** and **GG–1/2HCl** feature two isotropic peaks, corresponding to the amine and amide moieties (Table 5), with no apparent peaks corresponding to impurity phases. Interestingly, the two HCl salts feature similar chemical shifts for the amine nitrogen, with values of $\delta_{iso}(^{15}\mathrm{N})$ = 36.7 ppm for **GG–HCl–H$_2$O** and $\delta_{iso}(^{15}\mathrm{N})$ = 35.9 ppm for **GG–1/2HCl**, whereas the amine nitrogen in **GG** is more deshielded, with $\delta_{iso}(^{15}\mathrm{N})$ = 27.9 ppm. For the amide sites, the values of $\delta_{iso}(^{15}\mathrm{N})$ fall all within the narrow range of 113.1 to 117.4 ppm, with **GG** and **GG–1/2HCl** having the same isotropic chemical shift, to within experimental uncertainty. The amide chemical shift tensors for **GG** and **GG–1/2HCl** are also similar, but not identical, with Ω = 171.1 ppm and 176.4 ppm, respectively, and κ = −0.63 and −0.64, respectively. However, these values are markedly different for **GG–HCl–H$_2$O**, with Ω = 153.9 ppm and κ = −0.92.

The differences in the amide ^{15}N chemical shift tensors likely result from a number of factors, including the nature of

Table 5 Experimental and calculated ^{15}N chemical shift tensors[a,b,c,d]

			δ_{11} (ppm)	δ_{22} (ppm)	δ_{33} (ppm)	δ_{iso} (ppm)	Ω (ppm)	κ	d_ν (ppm)
GG	Amine	Exp.	34.9	27.9	20.9	27.9	14.0	0.00	—
		Calc.	34.3	30.4	24.0	29.6	10.3	0.24	1.9
	Amide	Exp.	220.8	81.7	49.7	117.4	171.1	−0.63	—
		Calc.	222.1	81.1	54.7	119.3	167.4	−0.68	2.4
GG–HCl–H$_2$O	Amine	Exp.	43.8	37.6	28.8	36.7	15.0	0.17	—
		Calc.	41.5	36.3	28.8	35.5	12.7	0.18	1.3
	Amide	Exp.	213.6	66.0	59.7	113.1	153.9	−0.92	—
		Calc.	216.9	68.7	59.4	115.0	157.5	−0.88	2.1
GG–1/2HCl	Amine	Exp.	42.6	38.7	26.4	35.9	16.2	0.52	—
		Calc.	40.5	37.9	28.7	35.7	11.8	0.56	1.2
	Amide	Exp.	224.4	79.8	48.0	117.4	176.4	−0.64	—
		Calc.	226.6	80.1	53.5	120.1	173.1	−0.69	3.0

[a] Calculated ^{15}N chemical shift tensors were obtained from DFT calculations on geometry optimized structures, performed at the PBE0-DH level in ORCA and ADF. [b] The principal components of the chemical shift tensors are defined using the frequency-ordered convention such that $\delta_{11} \geq \delta_{22} \geq \delta_{33}$. The isotropic chemical shift, span, and skew are given by $\delta_{iso} = (\delta_{11} + \delta_{22} + \delta_{33})/3$, $\Omega = \delta_{11} - \delta_{33}$, and $\kappa = 3(\delta_{22} - \delta_{iso})/\Omega$, respectively. [c] The chemical shift distance, d_ν, describes the agreement between experimental and calculated chemical shift tensors, as described in the SI (S1). [d] Uncertainties in each principal component are estimated to be ±1.0 ppm, based on bidirectional variation of Ω and κ.

 This journal is © the Owner Societies 2026

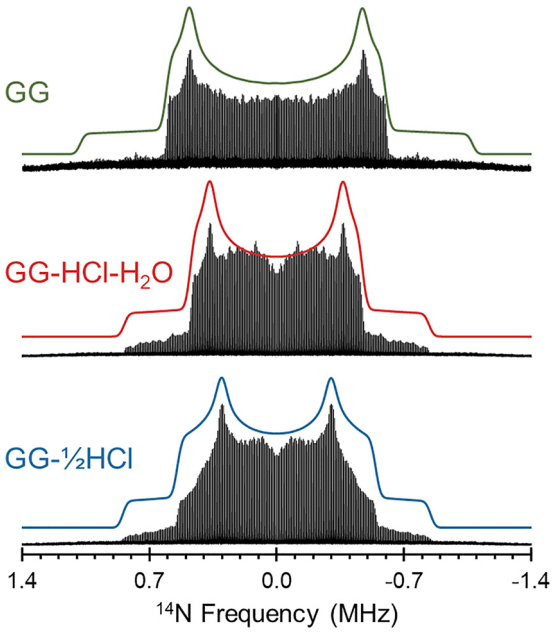


Fig. 6 $^{14}N\{^{1}H\}$ WURST-CPMG spectra acquired at 18.8 T (black) and corresponding analytical simulations (color).

Table 6 Experimental and calculated ^{14}N EFG tensors[a,b,c]

			C_Q (MHz)	η_Q
GG	Amine	Exp.	1.44(2)	0.12(2)
		Calc.	1.58	0.15
	Amide	Exp.	n/a	n/a
		Calc.	−3.12	0.52
GG–HCl–H_2O	Amine	Exp.	1.12(2)	0.13(2)
		Calc.	1.31	0.04
	Amide	Exp.	n/a	n/a
		Calc.	−3.49	0.51
GG–1/2HCl	Amine	Exp.	1.13(2)	0.29(2)
		Calc.	1.33	0.37
	Amide	Exp.	n/a	n/a
		Calc.	−3.11	0.60

[a] Theoretical EFG tensors were obtained from DFT calculations on geometry optimized structures, performed at the RPBE level in CASTEP. [b] The experimental uncertainties in the last digit for each value are indicated in parentheses. [c] The principal components of the EFG tensors are defined such that $|V_{33}| \geq |V_{22}| \geq |V_{11}|$. The quadrupolar coupling constant and asymmetry parameter are given by $C_Q = eQV_{33}/h$, and $\eta_Q = (V_{11} - V_{22})/V_{33}$, respectively. The sign of C_Q cannot be determined from the experimental ^{14}N spectra.

the hydrogen bonding network of the amide nitrogen and oxygen atoms.[52] In **GG–HCl–H_2O**, the amide nitrogen atom serves as a hydrogen bond donor to the chloride ion with a distance of $r(H\cdots Cl^-)$ = 2.39 Å, whereas in both **GG** and **GG–1/2HCl**, hydrogen bonds are formed between the amide proton and the amide oxygen atoms in another molecule with distances of $r(H\cdots O)$ = 2.03 Å and 1.93 Å, respectively. As a result, the amide chemical shift tensors in **GG** and **GG–1/2HCl** are very similar (*i.e.*, the largest difference in a principal component is 3.4 ppm, as seen in δ_{11}). The chemical shift tensor of **GG–HCl–H_2O** differs from the other solid forms, with substantial deviations observed for all three principal components.

The $^{14}N\{^{1}H\}$ WURST-CPMG spectra (Fig. 6) were acquired rapidly on stationary samples due to favorable relaxation characteristics of the protonated amine (RNH_3^+) sites (*i.e.*, short values of $T_1(^{14}N)$ that permit a short recycle delay, and long values of $T_2^{eff}(^{14}N)$ that provide S/N gains from the CPMG echo trains). The total pattern for each sample was produced by frequency-domain co-addition of seven individual subspectra that were acquired by stepping the transmitter in intervals of *ca.* 100 kHz in order to achieve uniform patterns. The appearances of these patterns are dominated by the first-order quadrupolar interaction, and are therefore expected to be symmetric. Therefore, only the positive frequency sides of the patterns were acquired, whereas the negative frequency sides were generated by mirroring the patterns about the Larmor frequency.[95]

The breadths of the ^{14}N powder patterns, and concomitant EFG tensor parameters, are consistent with previous reports related to protonated amine moieties in organic molecules.[96,143–146] There is no evidence of additional signals due to the amide moieties, which possibly reflects their anticipated large pattern breadths (*i.e.*, 4.7–5.2 MHz, corresponding to C_Q values of *ca.* 3.1–3.5 MHz, as predicted by DFT calculations), and/or unfavorable relaxation characteristics of these sites.[147,148]

The ^{14}N EFG tensors can be determined by resolving the positions of two key discontinuities in the ^{14}N powder pattern (Scheme S1).[95] This is readily accomplished by determining the positions of the "horn" and "shoulder" discontinuities (*i.e.*, ν_{11} and ν_{22}, respectively), since these are located in the highest signal intensity regions of the patterns, whereas the "foot" discontinuities (ν_{33}) are often difficult to resolve due to low S/N. The effects of ^{14}N chemical shift anisotropy (CSA) on these spectra is negligible, due to the dominant manifestation of the first-order quadrupolar interaction. In the case of **GG**, very little signal intensity is observed in the outer "feet" of the Pake-like doublet, likely due to reduced T_2^{eff} values for these isochromats; nonetheless, the positions of the two other discontinuities are all that is required to determine the values of C_Q and η_Q.[143]

The variation in the values of $C_Q(^{14}N)$ and η_Q for charged tertiary amines (Table 6) has been linked to the strength of intermolecular hydrogen bonds.[22,96,143–145] When these noncovalent interactions are absent, the value of η_Q approaches zero, indicating a near-axially symmetric ^{14}N EFG tensor with its largest component, V_{33}, oriented along or near the C–N bonding axis. However, when strong hydrogen bonds are present, the EFG tensor deviates from axial symmetry. In **GG**, the local environment consists of three $NH_3^+\cdots COO^-$ hydrogen bonds with distances between *ca.* 1.79 Å and 1.94 Å, according to the geometry optimized structure. As a consequence, the value of η_Q is low (0.12) and the value of C_Q is high (1.44 MHz), indicating that the EFGs along the C–N bonding axis are the highest in this series. For **GG–1/2HCl**, there is a single $NH_3^+\cdots Cl^-$ hydrogen bond (2.13 Å)—because this amine nitrogen features a uniquely anisotropic electronic environment, the value of η_Q is the highest for this series (0.29) and the value of C_Q is lower (1.13 MHz). For **GG–HCl–H_2O**, there is one $NH_3^+\cdots H_2O$ hydrogen bond (2.04 Å) and two $NH_3^+\cdots Cl^-$ hydrogen bonds, along with intermediate EFG tensor parameters of C_Q = 1.12 MHz and η_Q = 0.13.

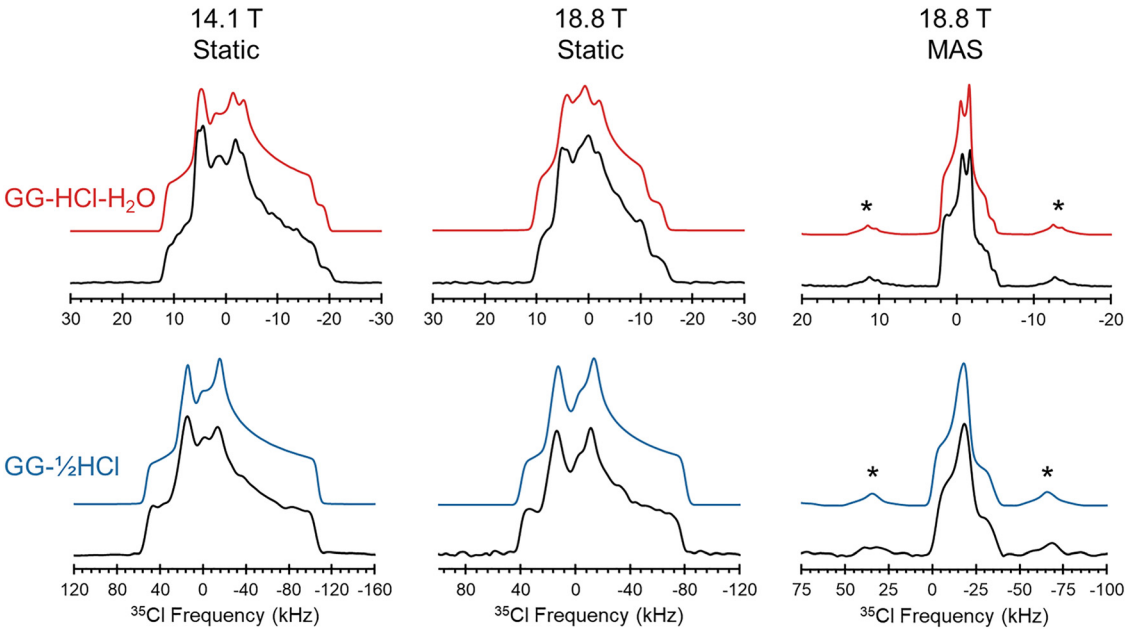


Fig. 7 $^{35}Cl\{^{1}H\}$ SSNMR spectra acquired under static conditions at 14.1 T and 18.8 T, and under MAS conditions at 18.8 T. Spinning side bands are marked by asterisks (*). Corresponding analytical simulations are shown in red or blue.

Table 7 Experimental and calculated ^{35}Cl EFG and chemical shift tensors[a,b,c,d,e,f]

		C_Q (MHz)	η_Q	δ_{iso} (ppm)	Ω (ppm)	κ	α (deg.)	β (deg.)	γ (deg.)
GG–HCl–H_2O	Exp.	2.89(3)	0.65(2)	28(2)	60(20)	0.7(3)	50(10)	45(5)	160(40)
	Calc.	−3.29	0.52	20	59	0.77	60	48	152
GG–1/2HCl	Exp.	6.48(4)	0.79(3)	−3(6)	200(50)	n/a[g]	n/a[g]	0(10)	n/a[g]
	Calc.	−7.11	0.74	11	217	−0.08	246	5	204

[a] Theoretical EFG and chemical shift tensor parameters were obtained from DFT calculations on geometry optimized structures, performed at the RPBE level in CASTEP. [b] The experimental uncertainties in the last digit for each value are indicated in parentheses. [c] The principal components of the EFG tensors are ranked $|V_{33}| \geq |V_{22}| \geq |V_{11}|$. The quadrupolar coupling constant and asymmetry parameter are defined as $C_Q = eQV_{33}/h$, and $\eta_Q = (V_{11} - V_{22})/V_{33}$, respectively. [d] The sign of C_Q cannot be determined from the experimental ^{35}Cl SSNMR spectra. [e] The principal components of the chemical shift tensors are defined using the frequency-ordered convention such that $\delta_{11} \geq \delta_{22} \geq \delta_{33}$. The isotropic chemical shift, span, and skew are given by $\delta_{iso} = (\delta_{11} + \delta_{22} + \delta_{33})/3$, $\Omega = \delta_{11} - \delta_{33}$, and $\kappa = 3(\delta_{22} - \delta_{iso})/\Omega$, respectively. [f] The Euler angles α, β, and γ define the relative orientation of the EFG and chemical shift tensors using the $ZY'Z''$ convention for rotation. The experimental angles derived from ssNake (which uses the $ZX'Z''$ convention) are adjusted to match the calculated values extracted by EFGShield. [g] This parameter has little or no discernible effect on the appearance of simulated powder patterns.

3.2.4 ^{35}Cl and $^{35}Cl \rightarrow {}^{1}H$ D-RINEPT spectra. $^{35}Cl\{^{1}H\}$ spectra were acquired at 14.1 T under static conditions and at 18.8 T under both static and MAS conditions (Fig. 7). The ^{35}Cl patterns are influenced by both the second-order quadrupolar and chemical shift interactions; thus, acquisition of spectra at multiple fields is necessary since their effects on the breadths of CT powder patterns scale in proportion to B_0^{-1} and B_0, respectively. Additionally, acquisition of patterns at 18.8 T under sufficiently fast MAS rates averages the effects of CSA on the isotropic centerband and partially averages second-order quadrupolar interaction effects. The combination of these three spectra provides the eight parameters necessary to fit each pattern, including the chemical shift (δ_{iso}; Ω; κ) and EFG (C_Q; η_Q) tensor parameters, and the three Euler angles (α; β; γ) defining the relative orientation of the principal axis systems of the EFG and chemical shift tensors (Table 7).

Each ^{35}Cl spectrum features a single pattern, which corresponds to the single crystallographically and magnetically distinct chloride ion site, consistent with the corresponding crystal structures. The patterns range in breadth between 160 kHz (**GG–1/2HCl**; 14.1 T; static) and 8 kHz (**GG–HCl–H_2O**; 18.8 T; MAS with ν_{rot} = 12 kHz). There are no impurity phases indicated in any of the spectra (including the absence of sharp peaks that may be indicative of unreacted educts or the decomposition and/or disproportionation products of the dipeptides).

The ^{35}Cl EFG tensors of chloride ions, and by extension, the appearance of their ^{35}Cl SSNMR powder patterns, are strongly influenced by the number, type, and spatial arrangement of hydrogen-bond donating moieties around the chloride ion (Table 8).[22,96,149–157] It is especially those $H\cdots Cl^-$ hydrogen bonds with $r(H\cdots Cl) \lesssim 2.2$ Å that most strongly influence ^{35}Cl

 This journal is © the Owner Societies 2026

Table 8 List of H···Cl⁻ contacts and calculated ^{35}Cl EFG tensor parameters for **GG–HCl–H$_2$O** and **GG–1/2HCl**

	Contact type[a]	H···Cl⁻ distance[b] (Å)	N–H···Cl⁻ angle[c] (°)	C_Q (MHz)	η_Q
GG–HCl–H$_2$O	H$_2$O···Cl⁻	2.164	162.2	−3.29	0.52
	NH_3^+···Cl⁻	2.288	149.8		
	NH_3^+···Cl⁻	2.297	152.7		
	Amide···Cl⁻	2.394	166.0		
GG–1/2HCl	NH_3^+···Cl⁻ (×2)	2.131	159.5	−7.11	0.74
	NH_3^+···Cl⁻ (×2)	2.895	116.0		

[a] Indicates the functional group involved in the H···Cl⁻ bond (*i.e.*, H$_2$O···Cl⁻ signifies a water contact, NH_3^+···Cl⁻ signifies a positively charged tertiary amine contact, and amide···Cl⁻ indicates an amide contact). [b] The shortest H···Cl⁻ hydrogen bonds, as determined from the geometry optimized crystal structures. [c] Angle between the hydrogen-bond donor atom, the hydrogen atom, and the chloride ion.

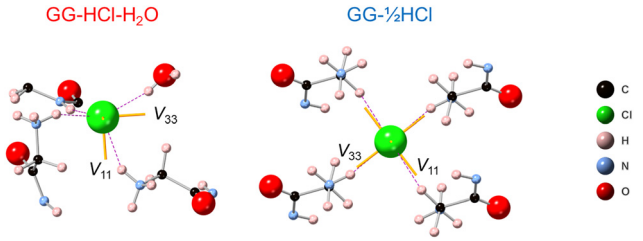


Fig. 8 ^{35}Cl EFG tensor orientations for the chloride ions in GG–HCl (left) and **GG–1/2HCl** (right). H···Cl⁻ hydrogen bonds are shown as dotted purple lines. The three yellow vectors represent the orientations of the principal components of the EFG tensors (V_{11}, V_{22}, and V_{33}), with V_{22} perpendicular to the page in each case.

EFG tensors.[149] The crystal structure of **GG–HCl–H$_2$O** features a single short contact with a water molecule, although the ^{35}Cl EFG tensor parameters (C_Q = 2.94 MHz; η_Q = 0.69) are more typical for those of a chloride ion featuring multiple hydrogen bonds with no short contacts—similar observations have been made for other systems in which the shortest hydrogen bond involves a water molecule, in which the orientation of the EFG tensor is not constrained by an obvious bonding or symmetry axis.[151] However, DFT calculations indicate that V_{33} is oriented in the general direction of the water contact in this case (Fig. 8). In contrast, the ^{35}Cl patterns and corresponding EFG tensor parameters for **GG–1/2HCl** (C_Q = 6.48 MHz; η_Q = 0.79) are highly unusual, resulting from the almost square-planar arrangement of hydrogen-bond donors around the chloride ion. DFT calculations show that this arrangement leads to large positive EFGs along the direction of the bonding axis of the short NH_3^+···Cl⁻ contact (*i.e.*, 2.131 Å), and large negative EFGs perpendicular to the plane. To the best of our knowledge, this is the first example of a chloride ion featuring both a high magnitude value of C_Q and a high value of η_Q, likely reflecting the uniqueness of the hydrogen bonding arrangement.

2D ^{35}Cl → ^{1}H D-RINEPT spectra were acquired with a spinning speed of ν_{rot} = 50 kHz and nine rotor periods of $SR4_2^1$ recoupling (Fig. 9). Similar to the 1D ^{35}Cl MAS spectra, the f_1 projection (*i.e.*, the ^{35}Cl dimension) indicates single CT patterns. The f_2 projection (*i.e.*, the ^{1}H dimension) features multiple peaks, corresponding to protons that are dipolar coupled to the chloride ions due to their spatial proximity. The ^{35}Cl → ^{1}H D-RINEPT spectrum of **GG–HCl–H$_2$O** features a broad peak that likely arises from the amine and amide moieties that participate in H···Cl⁻ hydrogen bonding; it is unclear whether or not a correlation with the water molecules is also indicated, as the δ_{iso}(^{1}H) also falls in this range. Interestingly, there is also a peak correlating to the ethylenic protons; this is likely because the shortest CH$_2$···Cl⁻ distance is only 2.938 Å. A peak arising from the carboxylic proton is also present, although it is less intense due to its greater distance from the chloride ion. The ^{35}Cl → ^{1}H D-RINEPT spectrum for **GG–1/2HCl** is remarkably different. Here, the crystal structure indicates that the chloride ion features hydrogen bonds with two protonated amine groups at distances of 2.131 Å, as well as two weaker contacts with protonated amine groups at 2.895 Å, all arranged in a plane. As a result, the D-RINEPT spectrum is

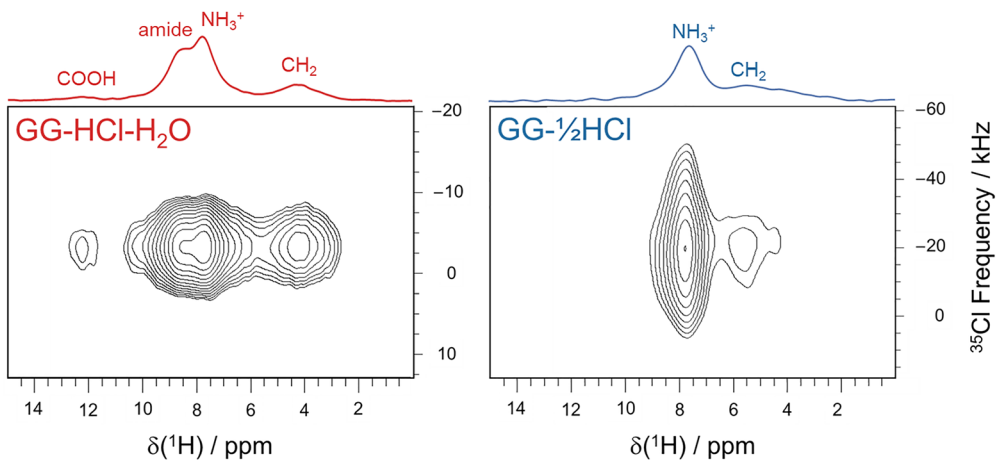


Fig. 9 2D ^{35}Cl → ^{1}H D-RINEPT correlation spectra acquired at 18.8 T with ν_{rot} = 50 kHz. A 1D cross-section is shown at the top of each spectrum, with ^{1}H peaks labeled with their respective moieties.

dominated by a single cross peak, corresponding to the interaction between the chloride ion and the protonated amine protons. There is also a much weaker peak that corresponds to ethylenic protons, the closest of which are 2.792 Å away. All of these observations are consistent with the crystal structures, and demonstrate the utility of 2D SSNMR methods for probing hydrogen bonding interactions in chloride salts.

3.3 DFT calculations of ^{13}C and ^{15}N magnetic shielding tensors

Quantum chemical calculations are critical for site assignment in SSNMR spectra and assessing chemical shift and EFG tensors in terms of molecular-level structure and bonding. In considering the various solid forms of glycylglycine, it is necessary to perform highly accurate calculations that reliably reproduce trends in the experimental NMR parameters. We employ the following protocols for calculating chemical shift and EFG tensors: (i) an initial structural model determined by SCXRD is subjected to a geometry optimization using dispersion-corrected plane-wave DFT in CASTEP, as described in Section 2.4; (ii) ^{14}N and ^{35}C EFG tensors are calculated using CASTEP; (iii) ^{1}H, ^{13}C, ^{15}N, and ^{35}Cl chemical shift tensors are computed using the GIPAW method within CASTEP using the RPBE functional; and (iv) ^{1}H, ^{13}C, and ^{15}N chemical shift tensors are calculated in ADF and ORCA using the geometry optimized structural models. The ADF calculations are performed using the following protocols: (a) clusters of up to fifteen molecules are used to account for lattice effects on the chemical shifts; (b) electrostatic embedding using COSMO is used to mimic interactions with more distant molecules; (c) the hybrid exchange–correlation functional PBE0 is used because of its ability to accurately model chemical shifts;[34–37] (d) the basis set TZ2P is used for the central molecule of the cluster, and DZP is used for all other molecules and chloride ions; and (c) a monomer correction is applied to the cluster-based (PBE0) calculations, which are performed at the PBE0-DH level. A summary of all experimental and calculated values used in this analysis is available in Table S8.

First, we comment on the accuracy of calculated ^{13}C and ^{15}N magnetic shielding tensors. Additional calculations were performed on glycine (α and γ polymorphs) and L-asparagine·H_2O, for the purpose of establishing correlation between experimental chemical shifts and calculated magnetic shieldings, as described through the linear correlation parameters A (slope of correlation line) and B (shielding of the reference state). The conversion of ^{13}C magnetic shielding tensors to the chemical shift scale should ideally feature a slope of $A = -1$ and a shielding for the reference state (neat TMS) of B = 186.4 ppm (obtained from measurement of the spin-rotation constant of ^{13}CO).[158] Similarly, for ^{15}N, the shielding of the reference state (neat nitromethane) is B = 264.5 ppm (obtained from measurement of the spin-rotation constant of $^{14}NH_3$).[159] However, the correlation between predicted magnetic shielding tensors and experimental chemical shift tensors can be improved by varying the parameters A and B to account for all types of systematic errors in the calculations.[160] Here, these values are optimized numerically *via* a generalized reduced gradient algorithm, as described in S1, with the goal of minimizing the root-mean-square chemical shift distance (Δ_{RMS}).[161]

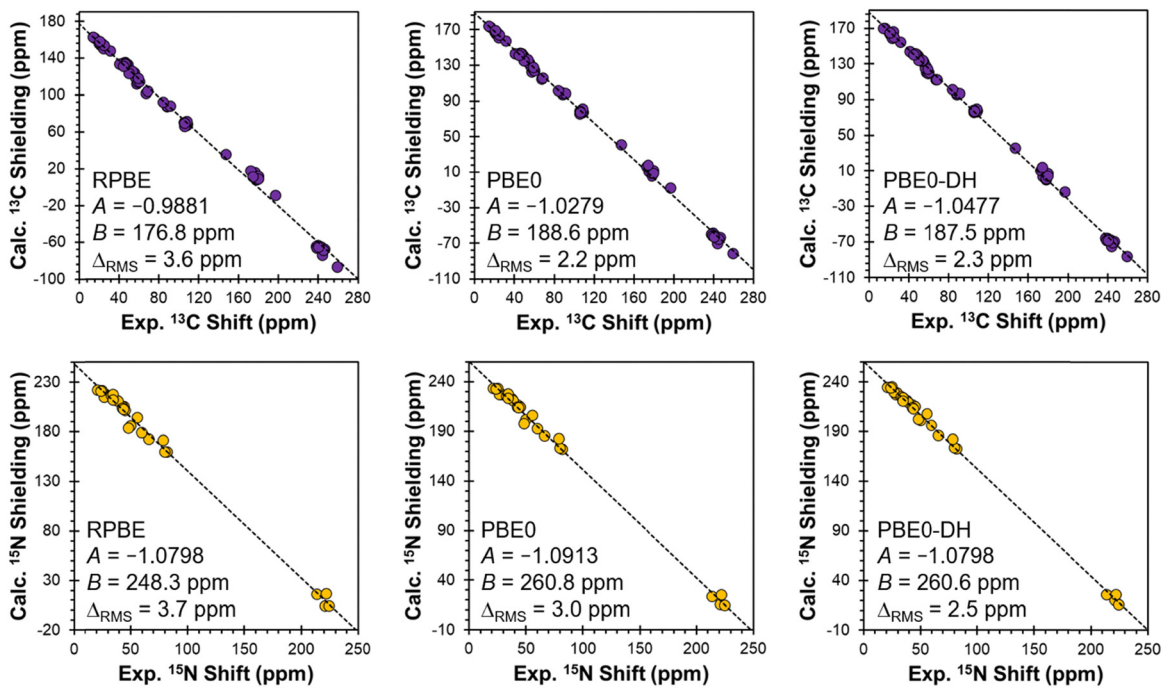


Fig. 10 Correlations between experimental principal values of ^{13}C and ^{15}N chemical shift tensors and principal values of calculated ^{13}C and ^{15}N magnetic shielding tensors. Calculations are performed at the RPBE/GIPAW, PBE0, and PBE0-DH levels. The dotted black lines are defined by the linear correlation parameters A and B. Errors in calculated values (relative to experiment) are given by the chemical shift distance.

 This journal is © the Owner Societies 2026

Three sets of calculations are presented and discussed for the prediction of ^{13}C and ^{15}N magnetic shielding tensors. These are RPBE/GIPAW calculations, cluster-based calculations using the PBE0 functional, and monomer corrections to the cluster-based calculations using the PBE0-DH functional. Fig. 10 shows correlations between experimental and calculated values of the principal components of the ^{13}C and ^{15}N chemical shift tensors for the three forms of glycylglycine (as well as L-asparagine·H_2O and two polymorphs of glycine), as computed using the RPBE/GIPAW method in CASTEP, the PBE0 method in ADF, and the PBE0-DH method in ADF and ORCA.

Statistical analysis indicates that the agreement between calculation and experiment depends critically on the level of DFT employed (Fig. 10). RPBE is a standard GGA functional, whereas PBE0 is a hybrid functional that includes 25% Hartree–Fock exchange, and PBE0-DH is a double-hybrid functional that includes 50% Hartree–Fock exchange and a 12.5% second-order Møller–Plesset correlation. For the ^{13}C chemical shift tensors, calculations at the PBE0 level lead to substantial improvement over those performed at the RPBE level, with chemical shift distances of $\Delta_{RMS}(^{13}C)$ = 2.2 ppm and 3.6 ppm, respectively. This trend is reproduced for the calculations of ^{15}N chemical shift tensors, with PBE0 calculations yielding $\Delta_{RMS}(^{15}N)$ = 3.0 ppm, and RPBE calculations yielding $\Delta_{RMS}(^{15}N)$ = 3.7 ppm. This result is also largely consistent with other studies that have found that calculations of chemical shift tensors performed using a hybrid functional provide better agreement with experiment than those performed with a GGA functional, albeit at a much higher computational cost for the former.[33] In contrast, the use of double hybrid functional approximations is less established for the prediction of chemical shifts or chemical shift tensors, with only a few examples in the current literature.[40,45] For this limited dataset, we find that use of the PBE0-DH functional leads to moderate improvement over PBE0 (especially for ^{15}N), with RMS chemical shift distances of $\Delta_{RMS}(^{13}C)$ = 2.3 ppm and $\Delta_{RMS}(^{15}N)$ = 2.5 ppm. It is also notable that use of the PBE0-DH functional leads to accurate shielding constants for the ^{13}C reference state of neat TMS (B = 187.5 ppm *vs.* the ideal value 186.4 ppm) and ^{15}N reference state of neat nitromethane (B = 260.6 ppm *vs.* the ideal value 249.9 ppm). Together, these computational results demonstrate the need for highly accurate DFT calculations of NMR parameters (using clusters of molecules and electrostatic embedding to model lattice effects, as well as expensive hybrid or double-hybrid functionals) to aid in the elucidation of crystal structures in NMRX studies.

4. Conclusion

This study has demonstrated a powerful multinuclear NMR crystallography approach for characterizing solid forms of organic solids. Multiple advanced SSNMR methods are used to provide a site-by-site analysis of all readily accessible NMR-active nuclides (*i.e.*, ^{1}H, ^{13}C, ^{15}N, ^{14}N, and ^{35}Cl), which in combination with X-ray diffraction measurements and state-of-the-art DFT calculations of NMR interaction tensors, provide a thorough description of electronic structure and bonding that is unrivaled by any other spectroscopic, spectrometric, or microscopic technique.

A novel salt of glycylglycine, **GG–1/2HCl**, was discovered, characterized by SCXRD and multinuclear SSNMR, and contrasted with known forms **GG** and **GG–HCl–H_2O**. **GG–1/2HCl** is unique in that it is a rare example of a hemihydrochloride salt of a peptide, and that the glycylglycine molecules dimerize through the formation of short single-well hydrogen bonds. Differences in structure and bonding between the three solid forms are readily apparent in their respective multinuclear SSNMR spectra, and reproduced through DFT calculations—measuring and calculating the ^{13}C and ^{15}N chemical shift tensors, as well as ^{14}N and ^{35}Cl EFG tensors, are particularly useful in this regard. Furthermore, direct spatial relationships between spins are observable in the 2D ^{1}H–^{1}H DQ–SQ spectra and $^{35}Cl \rightarrow {}^{1}H$ D-RINEPT spectra, providing additional metrics for validating structures. These methods have many potential applications to NMRX, including the determination of crystal structures through NMR-guided Rietveld refinement,[17] NMR-guided crystal structure prediction,[26] and even the structural characterization of amorphous solids.

Conflicts of interest

There are no conflicts to declare.

Data availability

The data supporting this article are included as part of the supplementary information (SI). Supplementary information: PXRD, additional SSNMR spectra and analysis, experimental parameters, results of DFT calculations. See DOI: https://doi.org/10.1039/d6cp02448c.

CCDC 2535045 contains the supplementary crystallographic data for this paper.[162]

Acknowledgements

This work was supported by the U.S. Department of Energy, Office of Science, Basic Energy Sciences, under Award DE-SC0022310. The authors are also grateful for support from The Florida State University and the National High Magnetic Field Laboratory, which is funded by the National Science Foundation Cooperative Agreement (NSF/DMR-2128556), and the State of Florida. R.J.I. acknowledges support from MRI CHE-1726824 and REU CHE-1950585. A portion of this research used resources provided by the X-ray Crystallography Center at the FSU Department of Chemistry and Biochemistry (FSU075000XRAY).

References

1 F. Taulelle, Fundamental Principles of NMR Crystallography, *eMagRes*, 2009.
2 S. E. Ashbrook and D. McKay, Combining solid-state NMR spectroscopy with first-principles calculations – a guide to

NMR crystallography, *Chem. Commun.*, 2016, **52**, 7186–7204.
3 P. Hodgkinson, NMR crystallography of molecular organics, *Prog. Nucl. Magn. Reson. Spectrosc.*, 2020, **118–119**, 10–53.
4 Z. Rehman, J. Lubay, W. T. Franks, A. P. Bartók, E. K. Corlett, B. Nguyen, G. Scrivens, B. M. Samas, H. Frericks-Schmidt and S. P. Brown, Organic NMR crystallography: enabling progress for applications to pharmaceuticals and plant cell walls, *Faraday Discuss.*, 2025, **255**, 222–243.
5 S. A. Ramos, L. J. Mueller and G. J. O. Beran, The interplay of density functional selection and crystal structure for accurate NMR chemical shift predictions, *Faraday Discuss.*, 2025, **255**, 119–142.
6 S. S. Gunaga, R. W. Schurko, S. T. Holmes and F. Mentink-Vigier, Accessible hybrid DFT-quality NMR crystallography via gas-phase machine learning interatomic potentials, *Chem. Sci.*, 2026.
7 K. Kalakewich, R. Iuliucci, K. T. Mueller, H. Eloranta and J. K. Harper, Monitoring the refinement of crystal structures with ^{15}N solid-state NMR shift tensor data, *J. Chem. Phys.*, 2015, **143**, 194702.
8 J. K. Harper, R. Iuliucci, M. Gruber and K. Kalakewich, Refining crystal structures with experimental ^{13}C NMR shift tensors and lattice-including electronic structure methods, *CrystEngComm*, 2013, **15**, 8693–8704.
9 R. Toomey, L. Wang, E. C. Heider, J. D. Hartman, A. J. Nichols, D. A. A. Myles, A. S. Gardberg, G. J. McIntyre, M. Zeller and M. A. Mehta, *et al.*, NMR-guided refinement of crystal structures using ^{15}N chemical shift tensors, *CrystEngComm*, 2024, **26**, 3289–3302.
10 S. T. Holmes, W. D. Wang, G. Hou, C. Dybowski, W. Wang and S. Bai, A new NMR crystallographic approach to reveal the calcium local structure of atorvastatin calcium, *Phys. Chem. Chem. Phys.*, 2019, **21**, 6319–6326.
11 E. Salager, R. S. Stein, C. J. Pickard, B. Elena and L. Emsley, Powder NMR crystallography of thymol, *Phys. Chem. Chem. Phys.*, 2009, **11**, 2610–2621.
12 J. K. Harper, A. E. Mulgrew, J. Y. Li, D. H. Barich, G. A. Strobel and D. M. Grant, Characterization of stereochemistry and molecular conformation using solid-state NMR tensors, *J. Am. Chem. Soc.*, 2001, **123**, 9837–9842.
13 C. Yang, L. Zhu, R. A. Kudla, J. D. Hartman, R. O. Al-Kaysi, S. Monaco, B. Schatschneider, A. Magalhães, G. J. O. Beran and C. J. Bardeen, *et al.*, Crystal structure of the metastable intermediate in the photomechanical, crystal-to-crystal reaction of 9-*tert*-butyl anthracene ester, *CrystEngComm*, 2016, **18**, 7319–7329.
14 C. J. H. Smalley, H. E. Hoskyns, C. E. Hughes, D. N. Johnstone, T. Willhammar, M. T. Young, C. J. Pickard, A. J. Logsdail, P. A. Midgley and K. D. M. Harris, A structure determination protocol based on combined analysis of 3D-ED data, powder XRD data, solid-state NMR data and DFT-D calculations reveals the structure of a new polymorph of l-tyrosine, *Chem. Sci.*, 2022, **13**, 5277–5288.
15 C. E. Hughes, G. N. M. Reddy, S. Masiero, S. P. Brown, P. A. Williams and K. D. M. Harris, Determination of a complex crystal structure in the absence of single crystals: analysis of powder X-ray diffraction data, guided by solid-state NMR and periodic DFT calculations, reveals a new 2′-deoxyguanosine structural motif, *Chem. Sci.*, 2017, **8**, 3971–3979.
16 J. K. Harper, D. H. Barich, E. M. Heider, D. M. Grant, R. R. Franke, J. H. Johnson, Y. Zhang, P. L. Lee, R. B. Von Dreele and B. Scott, *et al.*, A combined solid-state NMR and X-ray powder diffraction study of a stable polymorph of paclitaxel, *Cryst. Growth Des.*, 2005, **5**, 1737–1742.
17 C. S. Vojvodin, S. T. Holmes, C. E. A. Kirschhock, D. A. Hirsh, I. Huskić, S. Senanayake, L. Betancourt, W. Xu, E. Breynaert and T. Friščić, *et al.*, Rietveld refinement and NMR crystallographic investigations of multi-component crystals containing alkali metal chlorides and urea, *J. Appl. Crystallogr.*, 2025, **52**, 333–348.
18 J. K. Harper and D. M. Grant, Enhancing crystal-structure prediction with NMR tensor data, *Cryst. Growth Des.*, 2006, **6**, 2315–2321.
19 M. Baias, J.-N. Dumez, P. H. Svensson, S. Schantz, G. M. Day and L. Emsley, *De novo* determination of the crystal structure of a large drug molecule by crystal structure prediction-based powder NMR crystallography, *J. Am. Chem. Soc.*, 2013, **135**, 17501–17507.
20 M. Balodis, M. Cordova, A. Hofstetter, G. M. Day and L. Emsley, *De novo* crystal structure determination from machine learned chemical shifts, *J. Am. Chem. Soc.*, 2022, **144**, 7215–7223.
21 E. Salager, G. M. Day, R. S. Stein, C. J. Pickard, B. Elena and L. Emsley, Powder crystallography by combined crystal structure prediction and high-resolution ^{1}H solid-state NMR spectroscopy, *J. Am. Chem. Soc.*, 2010, **132**, 2564–2566.
22 C. H. Fleischer, S. T. Holmes, X. Lin and R. W. Schurko, *De novo* crystal structure determination of L-alaninamide HCl by quadrupolar NMR crystallography guided crystal structure prediction (QNMRX-CSP), *Solid State Nucl. Magn. Reson.*, 2025, **140**, 102034.
23 M. Cordova, P. Moutzouri, S. O. Nilsson Lill, A. Cousen, M. Kearns, S. T. Norberg, A. Svensk Ankarberg, J. McCabe, A. C. Pinon and S. Schantz, *et al.*, Atomic-level structure determination of amorphous molecular solids by NMR, *Nat. Commun.*, 2023, **14**, 5138.
24 M. Cordova, M. Balodis, A. Hofstetter, F. Paruzzo, S. O. Nilsson Lill, E. S. E. Eriksson, P. Berruyer, B. Simões de Almeida, M. J. Quayle and S. T. Norberg, *et al.*, Structure determination of an amorphous drug through large-scale NMR predictions, *Nat. Commun.*, 2021, **12**, 2964.
25 J. B. Holmes, D. Torodii, M. Balodis, M. Cordova, A. Hofstetter, F. Paruzzo, S. O. Nilsson Lill, E. Eriksson, P. Berruyer and B. Simões de Almeida, *et al.*, Atomic-level structure of the amorphous drug atuliflapon via NMR crystallography, *Faraday Discuss.*, 2024, 342–354.
26 A. A. Peach, C. H. Fleischer, K. Levin, S. T. Holmes, J. E. Sanchez and R. W. Schurko, Quadrupolar NMR crystallography guided crystal structure prediction (QNMRX-CSP), *CrystEngComm*, 2024, **26**, 4782–4803.

 This journal is © the Owner Societies 2026

27 C. Fleischer, S. T. Holmes, K. Levin, S. L. Veinberg and R. Schurko, Characterization of ephedrine HCl and pseudoephedrine HCl using quadrupolar NMR crystallography guided crystal structure prediction, *Faraday Discuss.*, 2025, 88–118.

28 D. M. Grant, F. Liu, R. J. Iuliucci, C. G. Phung, J. C. Facelli and D. W. Alderman, Relationship of ^{13}C NMR chemical shift tensors to diffraction structures, *Acta Crystallogr., Sect. B*, 1995, **51**, 540–546.

29 T. Charpentier, The PAW/GIPAW approach for computing NMR parameters: A new dimension added to NMR study of solids, *Solid State Nucl. Magn. Reson.*, 2011, **40**, 1–20.

30 C. Bonhomme, C. Gervais, F. Babonneau, C. Coelho, F. Pourpoint, T. Azaïs, S. E. Ashbrook, J. M. Griffin, J. R. Yates and F. Mauri, *et al.*, First-principles calculation of NMR parameters using the gauge including projector augmented wave method: a chemist's point of view, *Chem. Rev.*, 2012, **112**, 5733–5779.

31 M. Profeta, F. Mauri and C. J. Pickard, Accurate first principles prediction of ^{17}O NMR parameters in SiO_2: assignment of the zeolite ferrierite spectrum, *J. Am. Chem. Soc.*, 2003, **125**, 541–548.

32 S. T. Holmes, R. J. Iuliucci, K. T. Mueller and C. Dybowski, Density functional investigation of intermolecular effects on ^{13}C NMR chemical-shielding tensors modeled with molecular clusters, *J. Chem. Phys.*, 2014, **141**, 164121.

33 S. T. Holmes, R. J. Iuliucci, K. T. Mueller and C. Dybowski, Critical analysis of cluster models and exchange-correlation functionals for calculating magnetic shielding in molecular solids, *J. Chem. Theory Comput.*, 2015, **11**, 5229–5241.

34 S. T. Holmes, O. G. Engl, M. N. Srnec, J. D. Madura, R. Quiñones, J. K. Harper, R. W. Schurko and R. J. Iuliucci, Chemical shift tensors of cimetidine form A modeled with density functional theory calculations: implications for NMR crystallography, *J. Phys. Chem. A*, 2020, **124**, 3109–3119.

35 J. D. Hartman, R. A. Kudla, G. M. Day, L. J. Mueller and G. J. O. Beran, Benchmark fragment-based ^{1}H, ^{13}C, ^{15}N and ^{17}O chemical shift predictions in molecular crystals, *Phys. Chem. Chem. Phys.*, 2016, **18**, 21686–21709.

36 J. D. Hartman, G. M. Day and G. J. O. Beran, Enhanced NMR discrimination of pharmaceutically relevant molecular crystal forms through fragment-based *ab initio* chemical shift predictions, *Cryst. Growth Des.*, 2016, **16**, 6479–6493.

37 J. D. Hartman and G. J. O. Beran, Accurate ^{13}C and ^{15}N molecular crystal chemical shielding tensors from fragment-based electronic structure theory, *Solid State Nucl. Magn. Reson.*, 2018, **96**, 10–18.

38 J. D. Hartman, A. Balaji and G. J. O. Beran, Improved electrostatic embedding for fragment-based chemical shift calculations in molecular crystals, *J. Chem. Theory Comput.*, 2017, **13**, 6043–6051.

39 P. A. Unzueta and G. J. O. Beran, Polarizable continuum models provide an effective electrostatic embedding model for fragment-based chemical shift prediction in challenging systems, *J. Comput. Chem.*, 2020, **41**, 2251–2265.

40 S. T. Holmes, C. M. Boley, A. Dewicki, Z. T. Gardner, C. S. Vojvodin, R. J. Iuliucci and R. W. Schurko, Carbon-13 chemical shift tensor measurements for nitrogen-dense compounds, *Magn. Reson. Chem.*, 2024, **62**, 179–189.

41 P. Broqvist, A. Alkauskas and A. Pasquarello, Hybrid-functional calculations with plane-wave basis sets: Effect of singularity correction on total energies, energy eigenvalues, and defect energy levels, *Phys. Rev. B:Condens. Matter Mater. Phys.*, 2009, **80**, 085114.

42 M. Dračínský, P. Unzueta and G. J. O. Beran, Improving the accuracy of solid-state nuclear magnetic resonance chemical shift prediction with a simple molecular correction, *Phys. Chem. Chem. Phys.*, 2019, **21**, 14992–15000.

43 J. D. Hartman and J. K. Harper, Improving the accuracy of GIPAW chemical shielding calculations with cluster and fragment corrections, *Solid State Nucl. Magn. Reson.*, 2022, **122**, 101832.

44 T. Nakajima, An extrapolation scheme for solid-state NMR chemical shift calculations, *Chem. Phys. Lett.*, 2017, **677**, 99–106.

45 R. J. Iuliucci, J. D. Hartman and G. J. O. Beran, Do models beyond hybrid density functionals increase the agreement with experiment for predicted NMR chemical shifts or electric field gradient tensors in organic solids?, *J. Phys. Chem. A*, 2023, **127**, 2846–2858.

46 H. Brough, C. W. Cook, J. Griffin and M. J. G. Peach, Combining double-hybrid functionals with rSCAN yields solid-state ^{13}C chemical shifts with sub-ppm accuracy, *Phys. Chem. Chem. Phys.*, 2025, 15906–15919.

47 T. A. Cross and S. J. Opella, Solid-state NMR structural studies of peptides and proteins in membranes, *Curr. Opin. Struct. Biol.*, 1994, **4**, 574–581.

48 R. Tycko, Biomolecular solid state NMR: advances in structural methodology and applications to peptide and protein fibrils, *Annu. Rev. Phys. Chem.*, 2001, **52**, 575–606.

49 R. E. Stark, L. W. Jelinski, D. J. Ruben, D. A. Torchia and R. G. Griffin, ^{13}C chemical shift and ^{13}C-^{15}N dipolar tensors for the peptide bond: [1-^{13}C]glycyl[^{15}N]glycine·HCl·H_2O, *J. Magn. Reson.*, 1983, **55**, 266–273.

50 G. S. Harbison, L. W. Jelinski, R. E. Stark, D. A. Torchia, J. Herzfeld and R. G. Griffin, ^{15}N chemical shift and ^{15}N-^{13}C dipolar tensors for the peptide bond in [1-^{13}C]glycyl[^{15}N]-glycine hydrochloride monohydrate, *J. Magn. Reson.*, 1984, **60**, 79–82.

51 N. Takeda, S. Kuroki, H. Kurosu and I. Ando, ^{13}C-NMR chemical shift tensor and hydrogen-bonded structure of glycine-containing peptides in a single crystal, *Biopolymers*, 1999, **50**, 61–69.

52 A. Poon, J. Birn and A. Ramamoorthy, How does an amide-15N chemical shift tensor vary in peptides?, *J. Phys. Chem. B*, 2004, **108**, 16577–16585.

53 A. E. Walling, R. E. Pargas and A. C. de Dios, Chemical shift tensors in peptides: a quantum mechanical dtudy, *J. Phys. Chem. A*, 1997, **101**, 7299–7303.

54 X. Yao and M. Hong, Determination of Cα chemical shift tensor orientation in peptides by dipolar-modulated chemical shift recoupling NMR spectroscopy, *J. Am. Chem. Soc.*, 2002, **124**, 2730–2738.

55 M. Fritz, C. M. Quinn, M. Wang, G. Hou, X. Lu, L. M. I. Koharudin, J. Struppe, D. A. Case, T. Polenova and A. M. Gronenborn, Determination of accurate backbone chemical shift tensors in microcrystalline proteins by integrating MAS NMR and QM/MM, *Phys. Chem. Chem. Phys.*, 2018, **20**, 9543–9553.

56 Y. Wei, D.-K. Lee and A. Ramamoorthy, Solid-state ^{13}C NMR chemical shift anisotropy tensors of polypeptides, *J. Am. Chem. Soc.*, 2001, **123**, 6118–6126.

57 C. Ye, R. Fu, J. Hu, L. Hou and S. Ding, Carbon-13 chemical shift anisotropies of solid amino acids, *Magn. Reson. Chem.*, 1993, **31**, 699–704.

58 S. E. Soss, P. F. Flynn, R. J. Iuliucci, R. P. Young, L. J. Mueller, J. Hartman, G. J. O. Beran and J. K. Harper, Measuring and modeling highly accurate ^{15}N chemical shift tensors in a peptide, *ChemPhysChem*, 2017, **18**, 2225–2232.

59 R. H. Havlin, D. D. Laws, H.-M. L. Bitter, L. K. Sanders, H. Sun, J. S. Grimley, D. E. Wemmer, A. Pines and E. Oldfield, An experimental and theoretical investigation of the chemical shielding tensors of ^{13}Cα of alanine, valine, and leucine residues in solid peptides and in proteins in solution, *J. Am. Chem. Soc.*, 2001, **123**, 10362–10369.

60 Y. Wei, D.-K. Lee, A. E. McDermott and A. Ramamoorthy, A 2D MAS solid-state NMR method to recover the amplified heteronuclear dipolar and chemical shift anisotropic interactions, *J. Magn. Reson.*, 2002, **158**, 23–35.

61 D.-K. Lee, Y. Wei and A. Ramamoorthy, A two-dimensional magic-angle decoupling and magic-angle turning solid-state NMR method: an application to study chemical shift tensors from peptides that are nonselectively labeled with ^{15}N isotope, *J. Phys. Chem. B*, 2001, **105**, 4752–4762.

62 K. Loth, P. Pelupessy and G. Bodenhausen, Chemical shift anisotropy tensors of carbonyl, nitrogen, and amide proton nuclei in proteins through cross-correlated relaxation in NMR spectroscopy, *J. Am. Chem. Soc.*, 2005, **127**, 6062–6068.

63 K. Rübartsch, L. Hendrickx, E. Bartalucci, M. Plekhanov, M. Zobel, C. Bolm, M. Fyta and T. Wiegand, The accuracy of carbon-13 NMR magnetic-shielding tensors calculated using periodic DFT: a case study on the distinction of crystalline serine phases, *Phys. Chem. Chem. Phys.*, 2026, **28**, 5981–5991.

64 Z. Gu and A. McDermott, Chemical shielding anisotropy of protonated and deprotonated carboxylates in amino acids, *J. Am. Chem. Soc.*, 1993, **115**, 4282–4285.

65 R. Toomey, J. Powell, J. Cheever and J. K. Harper, Distinguishing between COOH, COO^-, and hydrogen disordered COOH sites in solids with ^{13}C chemical shift anisotropy and T_1 measurements, *Magn. Reson. Chem.*, 2024, **62**, 190–197.

66 C. M. Rienstra, L. Tucker-Kellogg, C. P. Jaroniec, M. Hohwy, B. Reif, M. T. McMahon, B. Tidor, T. Lozano-Pérez and R. G. Griffin, *De novo* determination of peptide structure with solid-state magic-angle spinning NMR spectroscopy, *Proc. Natl. Acad. Sci. U. S. A.*, 2002, **99**, 10260–10265.

67 B. J. Wylie, L. J. Sperling, A. J. Nieuwkoop, W. T. Franks, E. Oldfield and C. M. Rienstra, Ultrahigh resolution protein structures using NMR chemical shift tensors, *Proc. Natl. Acad. Sci. U. S. A.*, 2011, **108**, 16974–16979.

68 R. Parthasarathy, Crystal structure of glycylglycine hydrochloride, *Acta Crystallogr., Sect. B*, 1969, **25**, 509–518.

69 J. F. Griffin and P. Coppens, Valence electron distribution in perdeuterio-α-glycylglycine. high-resolution study of the peptide bond, *J. Am. Chem. Soc.*, 1975, **97**, 3496–3505.

70 E. Y. Chekmenev, K. W. Waddell, J. Hu, Z. Gan, R. J. Wittebort and T. A. Cross, Ion-binding study by ^{17}O solid-state NMR spectroscopy in the model peptide Gly-Gly-Gly at 19.6 T, *J. Am. Chem. Soc.*, 2006, **128**, 9849–9855.

71 J. Hu, E. Y. Chekmenev, Z. Gan, P. L. Gor'kov, S. Saha, W. W. Brey and T. A. Cross, Ion solvation by channel carbonyls characterized by ^{17}O solid-state NMR at 21 T, *J. Am. Chem. Soc.*, 2005, **127**, 11922–11923.

72 G. M. Sheldrick, A short history of SHELX, *Acta Crystallogr., Sect. A*, 2008, **64**, 112–122.

73 G. M. Sheldrick, Crystal structure refinement with SHELXL, *Acta Crystallogr., Sect. C*, 2015, **71**, 3–8.

74 O. V. Dolomanov, L. J. Bourhis, R. J. Gildea, J. A. K. Howard and H. Puschmann, OLEX2: a complete structure solution, refinement and analysis program, *J. Appl. Crystallogr.*, 2009, **42**, 339–341.

75 S. G. J. van Meerten, W. M. J. Franssen and A. P. M. Kentgens, ssNake: a cross-platform open-source NMR data processing and fitting application, *J. Magn. Reson.*, 2019, **301**, 56–66.

76 W. Sommer, J. Gottwald, D. E. Demco and H. W. Spiess, Dipolar heteronuclear multiple-quantum NMR spectroscopy in rotating solids, *J. Magn. Reson.*, 1995, **113**, 131–134.

77 I. Schnell, A. Lupulescu, S. Hafner, D. E. Demco and H. W. Spiess, Resolution enhancement in multiple-quantum MAS NMR spectroscopy, *J. Magn. Reson.*, 1998, **133**, 61–69.

78 Z. Gan, Rotary resonance echo double resonance for measuring heteronuclear dipolar coupling under MAS, *J. Magn. Reson.*, 2006, **183**, 235–241.

79 P. Moutzouri, B. Simões de Almeida, D. Torodii and L. Emsley, Pure isotropic proton solid state NMR, *J. Am. Chem. Soc.*, 2021, **143**, 9834–9841.

80 O. B. Peersen, X. L. Wu, I. Kustanovich and S. O. Smith, Variable-amplitude cross-polarization MAS NMR, *J. Magn. Reson.*, 1993, **104**, 334–339.

81 G. Metz, X. L. Wu and S. O. Smith, Ramped-amplitude cross polarization in magic-angle-spinning NMR, *J. Magn. Reson.*, 1994, **110**, 219–227.

82 J. Schaefer and E. O. Stejskal, Carbon-13 nuclear magnetic resonance of polymers spinning at the magic angle, *J. Am. Chem. Soc.*, 1976, **98**, 1031–1032.

 This journal is © the Owner Societies 2026

83 A. Pines, M. G. Gibby and J. S. Waugh, Proton-enhanced nuclear induction spectroscopy ^{13}C chemical shielding anisotropy in some organic solids, *Chem. Phys. Lett.*, 1972, **15**, 373–376.

84 A. Pines, M. G. Gibby and J. S. Waugh, Proton-enhanced NMR of dilute spins in solids, *J. Chem. Phys.*, 2003, **59**, 569–590.

85 S. R. Hartmann and E. L. Hahn, Nuclear double resonance in the rotating frame, *Phys. Rev.*, 1962, **128**, 2042–2053.

86 B. M. Fung, A. K. Khitrin and K. Ermolaev, An improved broadband decoupling sequence for liquid crystals and solids, *J. Magn. Reson.*, 2000, **142**, 97–101.

87 M. J. Potrzebowski, P. Tekely and Y. Dusausoy, Comment to ^{13}C-NMR studies of α and γ polymorphs of glycine, *Solid State Nucl. Magn. Reson.*, 1998, **11**, 253–257.

88 R. E. Taylor, ^{13}C CP/MAS: Application to glycine, *Concepts Magn. Reson., Part A*, 2004, **22A**, 79–89.

89 P. Bertani, J. Raya and B. Bechinger, ^{15}N chemical shift referencing in solid state NMR, *Solid State Nucl. Magn. Reson.*, 2014, **61–62**, 15–18.

90 M. Li, J. Li, X. Lu, R. Schroder, A. Chandramohan, W. P. Wuelfing, A. C. Templeton, W. Xu, M. Gindy and F. Kesisoglou, *et al.*, Molecular mechanism of P53 peptide permeation through lipid membranes from solid-state NMR spectroscopy and molecular dynamics simulations, *J. Am. Chem. Soc.*, 2024, **146**, 23075–23091.

91 L. A. O'Dell and R. W. Schurko, QCPMG using adiabatic pulses for faster acquisition of ultra-wideline NMR spectra, *Chem. Phys. Lett.*, 2008, **464**, 97–102.

92 L. A. O'Dell, A. J. Rossini and R. W. Schurko, Acquisition of ultra-wideline NMR spectra from quadrupolar nuclei by frequency stepped WURST–QCPMG, *Chem. Phys. Lett.*, 2009, **468**, 330–335.

93 R. Bhattacharyya and L. Frydman, Quadrupolar nuclear magnetic resonance spectroscopy in solids using frequency-swept echoing pulses, *J. Chem. Phys.*, 2007, **127**, 194503.

94 E. Kupce and R. Freeman, Adiabatic pulses for wideband inversion and broadband decoupling, *J. Magn. Reson.*, 1995, **115**, 273–276.

95 S. L. Veinberg, A. W. Lindquist, M. J. Jaroszewicz and R. W. Schurko, Practical considerations for the acquisition of ultra-wideline ^{14}N NMR spectra, *Solid State Nucl. Magn. Reson.*, 2017, **84**, 45–58.

96 S. T. Holmes, J. M. Hook and R. W. Schurko, Nutraceuticals in bulk and dosage forms: analysis by ^{35}Cl and ^{14}N solid-state NMR and DFT calculations, *Mol. Pharm.*, 2022, **19**, 440–455.

97 D. Massiot, I. Farnan, N. Gautier, D. Trumeau, A. Trokiner and J. P. Coutures, ^{71}Ga and ^{69}Ga nuclear magnetic resonance study of β-Ga_2O_3: resolution of four- and six-fold coordinated Ga sites in static conditions, *Solid State Nucl. Magn. Reson.*, 1995, **4**, 241–248.

98 A. Medek, V. Frydman and L. Frydman, Central transition nuclear magnetic resonance in the presence of large quadrupole couplings: cobalt-59 nuclear magnetic eesonance of cobaltophthalocyanines, *J. Phys. Chem. A*, 1999, **103**, 4830–4835.

99 E. L. Hahn, Spin echoes, *Phys. Rev.*, 1950, **80**, 580–594.

100 M. Goswami and P. K. Madhu, Sensitivity enhancement of the central-transition signal of half-integer spin quadrupolar nuclei in solid-state NMR: Features of multiple fast amplitude-modulated pulse transfer, *J. Magn. Reson.*, 2008, **192**, 230–234.

101 H.-T. Kwak, S. Prasad, T. Clark and P. J. Grandinetti, Enhancing sensitivity of quadrupolar nuclei in solid-state NMR with multiple rotor assisted population transfers, *Solid State Nucl. Magn. Reson.*, 2003, **24**, 71–77.

102 P. M. J. Szell and D. L. Bryce, Recent advances in chlorine, bromine, and iodine solid-state NMR spectroscopy, in *Annual Reports on NMR Spectroscopy*, ed. G. A. Webb, Academic Press, 2020, vol. 100, pp. 97–152.

103 J. Trebosc, B. Hu, J. P. Amoureux and Z. Gan, Through-space R^3-HETCOR experiments between spin-1/2 and half-integer quadrupolar nuclei in solid-state NMR, *J. Magn. Reson.*, 2007, **186**, 220–227.

104 A. Venkatesh, M. P. Hanrahan and A. J. Rossini, Proton detection of MAS solid-state NMR spectra of half-integer quadrupolar nuclei, *Solid State Nucl. Magn. Reson.*, 2017, **84**, 171–181.

105 A. Brinkmann and A. P. M. Kentgens, Proton-selective ^{17}O–^{1}H distance measurements in fast magic-angle-spinning solid-state NMR spectroscopy for the determination of hydrogen bond lengths, *J. Am. Chem. Soc.*, 2006, **128**, 14758–14759.

106 S. J. Clark, M. D. Segall, C. J. Pickard, P. J. Hasnip, M. J. Probert, K. Refson and M. C. Payne, First principles methods using CASTEP, *Z. Kristallogr.*, 2005, **220**, 567–570.

107 B. Hammer, L. B. Hansen and J. K. Nørskov, Improved adsorption energetics within density-functional theory using revised Perdew-Burke-Ernzerhof functionals, *Phys. Rev. B:Condens. Matter Mater. Phys.*, 1999, **59**, 7413–7421.

108 J. R. Yates, C. J. Pickard and F. Mauri, Calculation of NMR chemical shifts for extended systems using ultrasoft pseudopotentials, *Phys. Rev. B:Condens. Matter Mater. Phys.*, 2007, **76**, 024401.

109 H. J. Monkhorst and J. D. Pack, Special points for Brillouin-zone integrations, *Phys. Rev. B*, 1976, **13**, 5188–5192.

110 B. G. Pfrommer, M. Côté, S. G. Louie and M. L. Cohen, Relaxation of crystals with the quasi-Newton method, *J. Comput. Phys.*, 1997, **131**, 233–240.

111 S. Grimme, Semiempirical GGA-type density functional constructed with a long-range dispersion correction, *J. Comput. Chem.*, 2006, **27**, 1787–1799.

112 E. R. McNellis, J. Meyer and K. Reuter, Azobenzene at coinage metal surfaces: role of dispersive van der Waals interactions, *Phys. Rev. B:Condens. Matter Mater. Phys.*, 2009, **80**, 205414.

113 S. T. Holmes, R. J. Iuliucci, K. T. Mueller and C. Dybowski, Semi-empirical refinements of crystal structures using ^{17}O quadrupolar-coupling tensors, *J. Chem. Phys.*, 2017, **146**, 064201.

114 S. T. Holmes and R. W. Schurko, Refining crystal structures with quadrupolar NMR and dispersion-corrected

density functional theory, *J. Phys. Chem. C*, 2018, **122**, 1809–1820.
115 S. T. Holmes, C. S. Vojvodin and R. W. Schurko, Dispersion-corrected DFT methods for applications in nuclear magnetic resonance crystallography, *J. Phys. Chem. A*, 2020, **124**, 10312–10323.
116 S. Grimme, Semiempirical hybrid density functional with perturbative second-order correlation, *J. Chem. Phys.*, 2006, **124**, 034108.
117 L. Goerigk and S. Grimme, Efficient and accurate double-hybrid-meta-GGA density functionals—evaluation with the extended GMTKN30 database for general main group thermochemistry, kinetics, and noncovalent interactions, *J. Chem. Theory Comput.*, 2010, **7**, 291–309.
118 S. Grimme, S. Ehrlich and L. Goerigk, Effect of the damping function in dispersion corrected density functional theory, *J. Comput. Chem.*, 2011, **32**, 1456–1465.
119 C. J. Pickard and F. Mauri, All-electron magnetic response with pseudopotentials: NMR chemical shifts, *Phys. Rev. B:Condens. Matter Mater. Phys.*, 2001, **63**, 245101–245113.
120 J. R. Yates, C. J. Pickard and F. Mauri, Calculation of NMR chemical shifts for extended systems using ultrasoft pseudopotentials, *Phys. Rev. B:Condens. Matter Mater. Phys.*, 2007, **76**, 024401.
121 *ADF 2021.1*; SCM, Theoretical Chemistry, Vrije Universiteit, Amsterdam, The Netherlands, 2021. (accessed.
122 C. Adamo and V. Barone, Toward reliable density functional methods without adjustable parameters: the PBE0 model, *J. Chem. Phys.*, 1999, **110**, 6158–6170.
123 E. v Lenthe, E. J. Baerends and J. G. Snijders, Relativistic regular two-component Hamiltonians, *J. Chem. Phys.*, 1993, **99**, 4597–4610.
124 A. D. Becke, A multicenter numerical integration scheme for polyatomic molecules, *J. Chem. Phys.*, 1988, **88**, 2547–2553.
125 M. Franchini, P. H. T. Philipsen and L. Visscher, The Becke fuzzy cells integration scheme in the Amsterdam Density Functional program suite, *J. Comput. Chem.*, 2013, **34**, 1819–1827.
126 A. Klamt and G. Schüürmann, COSMO: a new approach to dielectric screening in solvents with explicit expressions for the screening energy and its gradient, *J. Chem. Soc., Perkin Trans. 2*, 1993, 799–805.
127 A. Klamt, Conductor-like screening model for real solvents: a new approach to the quantitative calculation of solvation phenomena, *J. Phys. Chem.*, 1995, **99**, 2224–2235.
128 A. Klamt and V. Jonas, Treatment of the outlying charge in continuum solvation models, *J. Chem. Phys.*, 1996, **105**, 9972–9981.
129 A. Klamt, C. Moya and J. Palomar, A comprehensive comparison of the IEFPCM and SS(V)PE continuum solvation methods with the COSMO approach, *J. Chem. Theory Comput.*, 2015, **11**, 4220–4225.
130 C. C. Pye and T. Ziegler, An implementation of the conductor-like screening model of solvation within the Amsterdam density functional package, *Theor. Chem. Acc.*, 1999, **101**, 396–408.
131 B. Delley, The conductor-like screening model for polymers and surfaces, *Mol. Simul.*, 2006, **32**, 117–123.
132 N. L. Allinger, X. Zhou and J. Bergsma, Molecular mechanics parameters, *J. Mol. Struct. THEOCHEM*, 1994, **312**, 69–83.
133 F. Neese, The ORCA program system, *Wiley Interdiscip. Rev.: Comput. Mol. Sci.*, 2012, **2**, 73–78.
134 G. L. Stoychev, A. A. Auer, R. Izsák and F. Neese, Self-consistent field calculation of nuclear magnetic resonance chemical shielding constants using gauge-including atomic orbitals and approximate two-electron integrals, *J. Chem. Theory Comput.*, 2018, **14**, 619–637.
135 G. L. Stoychev, A. A. Auer and F. Neese, Efficient and accurate prediction of nuclear magnetic resonance shielding tensors with double-hybrid density functional theory, *J. Chem. Theory Comput.*, 2018, **14**, 4756–4771.
136 E. Brémond and C. Adamo, Seeking for parameter-free double-hybrid functionals: the PBE0-DH model, *J. Chem. Phys.*, 2011, **135**, 024106.
137 F. Jensen, Segmented Contracted Basis Sets Optimized for Nuclear Magnetic Shielding, *J. Chem. Theory Comput.*, 2015, **11**, 132–138.
138 S. Kossmann and F. Neese, Efficient structure optimization with second-order many-body perturbation theory: the RIJCOSX-MP2 method, *J. Chem. Theory Comput.*, 2010, **6**, 2325–2338.
139 C. Hättig, Optimization of auxiliary basis sets for RI-MP2 and RI-CC2 calculations: core–valence and quintuple-ζ basis sets for H to Ar and QZVPP basis sets for Li to Kr, *Phys. Chem. Chem. Phys.*, 2005, **7**, 59–66.
140 C. Sabena, C. Rosso, T. Iftemie, R. Gobetto, D. L. Bryce and M. R. Chierotti, Solid-state NMR characterization of weak interactions in molecular crystals, *Coord. Chem. Rev.*, 2026, **555**, 217610.
141 L. A. O'Dell, Direct detection of nitrogen-14 in solid-state NMR spectroscopy, *Prog. Nucl. Magn. Reson. Spectrosc.*, 2011, **59**, 295–318.
142 S. Cavadini, S. Antonijevic, A. Lupulescu and G. Bodenhausen, Indirect detection of nitrogen-14 in solid-state NMR spectroscopy, *ChemPhysChem*, 2007, **8**, 1363–1374.
143 S. L. Veinberg, Z. W. Friedl, A. W. Lindquist, B. Kispal, K. J. Harris, L. A. O'Dell and R. W. Schurko, ^{14}N solid-state NMR spectroscopy of amino acids, *ChemPhysChem*, 2016, **17**, 4011–4027.
144 S. L. Veinberg, K. E. Johnston, M. J. Jaroszewicz, B. M. Kispal, C. R. Mireault, T. Kobayashi, M. Pruski and R. W. Schurko, Natural abundance ^{14}N and ^{15}N solid-state NMR of pharmaceuticals and their polymorphs, *Phys. Chem. Chem. Phys.*, 2016, **18**, 17713–17730.
145 S. L. Veinberg, Z. W. Friedl, K. J. Harris, L. A. O'Dell and R. W. Schurko, Ultra-wideline ^{14}N solid-state NMR as a method for differentiating polymorphs: glycine as a case study, *CrystEngComm*, 2015, **17**, 5225–5236.
146 L. A. O'Dell and R. W. Schurko, Static solid-state ^{14}N NMR and computational studies of nitrogen EFG tensors in some crystalline amino acids, *Phys. Chem. Chem. Phys.*, 2009, **11**, 7069–7077.

 This journal is © the Owner Societies 2026

147 H. Chihara and N. Nakamura, *Nuclear Quadrupole Resonance Spectroscopy Data*, Springer-Verlag, Berlin, 1997.
148 T. Das and E. L. Hahn, *Nuclear Quadrupole Resonance Spectroscopy*, Academic Press, 1958.
149 H. Hamaed, J. M. Pawlowski, B. F. T. Cooper, R. Fu, S. H. Eichhorn and R. W. Schurko, Application of solid-state ^{35}Cl NMR to the structural characterization of hydrochloride pharmaceuticals and their polymorphs, *J. Am. Chem. Soc.*, 2008, **130**, 11056–11065.
150 M. Hildebrand, H. Hamaed, A. M. Namespetra, J. M. Donohue, R. Fu, I. Hung, Z. Gan and R. W. Schurko, ^{35}Cl solid-state NMR of HCl salts of active pharmaceutical ingredients: structural prediction, spectral fingerprinting and polymorph recognition, *CrystEngComm*, 2014, **16**, 7334–7356.
151 S. T. Holmes, C. S. Vojvodin, N. Veinberg, E. M. Iacobelli, D. A. Hirsh and R. W. Schurko, Hydrates of active pharmaceutical ingredients: A ^{35}Cl and ^{2}H solid-state NMR and DFT study, *Solid State Nucl. Magn. Reson.*, 2022, **122**, 101837.
152 C. S. Vojvodin, S. T. Holmes, L. K. Watanabe, J. M. Rawson and R. W. Schurko, Multi-component crystals containing urea: mechanochemical synthesis and characterization by ^{35}Cl solid-state NMR spectroscopy and DFT calculations, *CrystEngComm*, 2022, **24**, 2626–2641.
153 A. A. Peach, D. A. Hirsh, S. T. Holmes and R. W. Schurko, Mechanochemical syntheses and ^{35}Cl solid-state NMR characterization of fluoxetine HCl cocrystals, *CrystEngComm*, 2018, **20**, 2780–2792.
154 Z. T. Dowdell, A. A. Peach, J. P. Purdie, S. T. Holmes, L. K. Watanabe, J. M. Rawson and R. W. Schurko, Mechanochemical synthesis and ^{35}Cl NMR crystallography of ionic cocrystals of phenothiazine drugs, *CrystEngComm*, 2025, **27**, 3752–3768.
155 L. M. Abdulla, A. A. Peach, S. T. Holmes, Z. T. Dowdell, L. K. Watanabe, E. M. Iacobelli, D. A. Hirsh, J. M. Rawson and R. W. Schurko, Synthesis and characterization of xylazine hydrochloride Polymorphs, hydrates, and cocrystals: a ^{35}Cl solid-state NMR and DFT study, *Crystal Growth Des.*, 2023, **23**, 3412–3426.
156 C. S. Vojvodin, J. E. Sanchez, S. T. Holmes, X. Lin and R. W. Schurko, Mechanochemical synthesis and NMR crystallography of multicomponent crystals: new perspectives from chlorine and alkali metal solid-state NMR spectroscopy, *Crystal Growth Des.*, 2025, **25**, 9591–9609.
157 C. H. Fleischer, V. K. Rash, Z. T. Dowdell, S. Termos, X. Lin, S. S. Gunaga, F. Mentink-Vigier, J. Jimenez, A. M. M. Abeykoon and S. Senanayake, *et al.*, Multinuclear solid-state NMR and NMR crystallography of solid forms of creatine and creatinine, *Mol. Pharm.*, 2026, 3397–3409.
158 A. K. Jameson and C. J. Jameson, Gas-phase ^{13}C chemical shifts in the zero-pressure limit: refinements to the absolute shielding scale for ^{13}C, *Chem. Phys. Lett.*, 1987, **134**, 461–466.
159 C. J. Jameson, A. K. Jameson, D. Oppusunggu, S. Wille, P. M. Burrell and J. Mason, ^{15}N nuclear magnetic shielding scale from gas phase studies, *J. Chem. Phys.*, 1981, **74**, 81–88.
160 M. H. Sherwood, J. C. Facelli, D. W. Alderman and D. M. Grant, Carbon-13 chemical shift tensors in polycyclic aromatic compounds. 2. single-crystal study of naphthalene, *J. Am. Chem. Soc.*, 1991, **113**, 750–753.
161 D. W. Alderman, M. H. Sherwood and D. M. Grant, Comparing, modeling, and assigning chemical-shift tensors in the cartesian, irreducible spherical, and icosahedral representations, *J. Magn. Reson.*, 1993, **101**, 188–197.
162 CCDC 2535045: Experimental Crystal Structure Determination, 2026, DOI: 10.5517/ccdc.csd.cc2r2xnf.